December 1992          *THESIS*

Wind Profiling in a Cloudy Convective Atmospheric
Boundary Layer Over Land

Captain David A. Valler Jr.

AFIT Student Attending:   Pennsylvania State University     AFIT/CI/CIA- 92-113

AFIT/CI
Wright-Patterson AFB OH 45433-6583

**DTIC**
**S** **ELECTE**
JUN 4 1993
**C** **D**

Approved for Public Release IAW 190-1
Distributed Unlimited
ERNEST A. HAYGOOD, Captain,. USAF
Executive Officer

90

113

The Pennsylvania State University

The Graduate School

# WIND PROFILING IN A CLOUDY CONVECTIVE ATMOSPHERIC BOUNDARY LAYER OVER LAND

A Thesis in

Meteorology

by

David A. Valler Jr.

DTIC QUALITY INSPECTED 5

Submitted in Partial Fulfillment
of the Requirements
for the Degree of

Master of Science

December 1992

| Accesion For | | |
|---|---|---|
| NTIS CRA&I | ☑ | |
| DTIC TAB | ☐ | |
| Unannounced | ☐ | |
| Justification | | |
| By | | |
| Distribution / | | |
| Availability Codes | | |
| Dist | Avail and / or Special | |
| A-1 | | |

DTIC QUALITY INSPECTED 5

93-12510

93 6 03 021

I grant The Pennsylvania State University the nonexclusive
right to use this work for the University's own purposes and
to make single copies of the work available to the public on
a not-for-profit basis if copies are not otherwise available.


David A. Valler Jr.

We approve the thesis of David A. Valler Jr.

Date of Signature

_Bruce A. Albrecht_ (signature)                    14 August 1992

Bruce A. Albrecht
Professor of Meteorology
Thesis Advisor


_George S. Young_ (signature)                    18 August 1992

George S. Young
Associate Professor of Meteorology


_Dennis W. Thomson_ (signature)                    19 August 1992

Dennis W. Thomson
Professor of Meteorology
Head of the Department of Meteorology

ABSTRACT

The vertical velocity structure of a cloud-topped atmospheric boundary layer, over land, was evaluated using high temporal vertical velocity measurements from two UHF clear-air Doppler radars (wind profilers) on 20 March 1991 and 31 January 1992, located at Penn State's Circleville Farm site. On both dates, post-cold-frontal stratocumulus covered the area. A transition from a cloudy convective boundary layer to a clear convective boundary layer occurred on 20 March 1991.

Vertical velocities were measured, at 30-second intervals, using the vertical beam of the profilers. Vertical velocities were averaged over hourly periods. Vertical velocity variance, Signal-to-Noise Ratio (SNR), and SNR variance were also evaluated for each hourly period.

The 915 MHz wind profiler proved to be extremely sensitive to the presence of precipitation. As a result of an angular bias in the vertical beam, vertical velocities measured with the 915 MHz wind profiler were also sensitive to horizontal winds. In addition, the so-called zero suppression filtering biased the 915 MHz profiler measurements obtained on 20 March 1991. The 404 MHz profiler measured vertical velocities at 30-second intervals on 20 March 1991 only.

Large downward vertical velocities and peaks in vertical velocity variance were observed at cloud top. These were,

possibly, the result of highly scattering inverted cloud top-related plumes. Boundary layer air and entrained free atmosphere air mixed in the inverted plume would produce an enhanced structure function parameter ($C_n^2$), on which the radar reflectivity depends. The signal processing "peak-picking" routine would thus pick the power peak of the more highly scattering inverted plume, rather than that of the weaker, compensating upward vertical velocities. When cloud cover decreased, strong upward velocities were preferentially measured in the lower boundary layer, perhaps as a result of high $C_n^2$ in the plumes generated by surface heating.

TABLE OF CONTENTS

LIST OF FIGURES

LIST OF TABLES

# Chapter 1

## INTRODUCTION

Large areas of stratocumulus clouds are commonly observed over land behind cold frontal systems and over the eastern regions of subtropical oceanic high pressure regions over oceans (Schubert et al., 1979; Brost et al., 1982; Albrecht et al., 1985). The eastern Pacific, off the California coast, for example, is an area of persistent formation. A convective boundary layer topped by stratocumulus is also commonly observed after frontal passages. These stratocumulus-covered areas substantially impact the earth's overall energy budget by reflecting incoming solar radiation. The importance of these boundary layer clouds has stimulated new research into the structure of the cloud-topped boundary layer. It has been a subject of interest since Lilly's (1968) pioneering work. Measurements of the stratocumulus structure help, in particular, to assess the impact of stratocumulus-topped boundary layers on the earth's overall heat budget.

## 1.1 Cloud-Topped Boundary Layer Modeling

Modeling can provide unique insight into the structure of cloud-topped mixed layers. It also allows researchers a means of studying boundary layer structure over a wide range of conditions. The introductory work by Lilly (1968) outlined

the significance of stratocumulus capped convective boundary layers and the limitations, at that time, of cloud-topped mixed layer modeling. To close Lilly's equations, maximum and minimum limits on entrainment were theorized from turbulent energy balances. Schubert (1976) later experimented with Lilly's mixed layer model. He used a weighted average of Lilly's maximum and minimum entrainment conditions. Diurnal variations evident in the mixed layer model output indicated a need for observational data to verify its performance. Deardorff (1980) modeled stratocumulus topped boundary layers to investigate the importance of cloud top radiative cooling. Vertical velocity variance within the capping inversion was enhanced by evaporative cooling of air from the free atmosphere above the inversion. When scaled by the convective velocity scale ($w_*$), the vertical velocity variance in a cloud-topped mixed layer was found to have a value larger than that under clear sky conditions. Later, using large eddy simulations, Moeng (1986) addressed the relationship between surface heating and cloud top cooling. The vertical velocity variance was decomposed into a contribution from cloud-top radiative cooling, and another from surface heating. The height of the variance maximum can be related to the ratio of cloud-top cooling to surface heating. Moeng (1987) also studied the distribution of radiative cooling at cloud top and determined that 85% of the radiative cooling occurred within the statically stable entrainment zone (The zone at the top of

the mixed layer where the buoyancy flux is negative).

## 1.2  Doppler Wind Profiling

The variability of vertical motions in a cloud-topped boundary layer is a means of inferring the location of increased turbulence.  Solar heating of the earth's surface provides buoyant production of turbulent kinetic energy.  It results in a maximum in the vertical velocity variance at about half the boundary layer depth.  Cloud top radiative cooling, another source of turbulent energy, is also marked by an increase in the vertical velocity variance in the mixed layer.  The height of the peak in the vertical velocity variance is an indication of the relative strength between buoyant production and cloud top radiative cooling (Moeng, 1986).  In addition, cloud-topped radiative cooling induces a secondary peak in vertical velocity variance at cloud top (Deardorff, 1980).

Measurements of the atmospheric boundary layer help to substantiate the physical parameterizations used in the models.  Boundary layer wind profilers have given experimentalists, and modelers alike, access to high temporal resolution wind data.  Vertical wind velocity can be measured by Doppler wind profilers that sense the irregularities in the radio refractive index of the clear atmosphere.  Proper frequency selection can minimize contamination from

precipitation. Some direct measurements of vertical air velocity can be made using a vertically pointing zenith beam of a wind profiler. However, the extent to which one can trust these data strongly depends on the angular bias in the zenith beam and the magnitude and the direction of the horizontal wind in the layer being measured.

## 1.3   Purpose of this Thesis

In this thesis, I outline a method for using clear-air Doppler radars (404 MHz & 915 MHz) in a cloudy convective boundary layer, over land, to determine cloud and sub-cloud vertical velocity structure, and evaluate the performance of two different wind profilers for this purpose. In chapter 2, I provide background information on the structure of stratocumulus-topped boundary layers. Chapter 3 includes instrument descriptions, and theory of Doppler wind profilers. Some theoretical limitations caused by horizontal wind contamination and precipitation contamination will be presented. Chapter 4 combines a discussion of data processing and filtering with data observations and observed instrument limitations. The results of data analysis are also contained in chapter 4. In chapter 5, I present my conclusions and identify some future work that will be necessary if Doppler wind profilers are to be used to measure the velocity structure in cloud-topped convective boundary layers.

Chapter 2

CLOUD-TOPPED ATMOSPHERIC BOUNDARY LAYER

## 2.1  Lilly's Model

In a clear convective boundary layer, the surface flux of potential temperature $\overline{(w'\theta')}_s$, is regarded as the primary mechanism for generating atmospheric boundary layer turbulence. Thermals of warm air rise from the sun-heated surface and thus generate turbulence in the boundary layer. On the other hand, in a cloudy convective boundary layer, cloud top radiative cooling is believed to be the principle generation mechanism of turbulence (Lilly, 1968; Moeng, 1987). Radiative cooling creates zones of cool, sinking air near cloud top. In essence, these "upside-down" thermals generated at cloud top appear to be analogous to the more familiar thermals generated by convection near the surface (Hignett, 1991). Also, in a relatively more stable cloudy boundary layer, shear generated mechanical turbulence can be significant.

Broken to overcast stratocumulus clouds provide sufficient cloud coverage in a convective boundary layer to minimize the need for surface buoyancy as a driving mechanism. With solid clouds, the radiative cooling at cloud top may be sufficient to force the mixing needed to maintain these clouds. When Lilly (1968) considered the radiative balance of

stratocumulus, he theorized that the stratocumulus deck would act as a black body when the cloud layer was at least 125m to 150m thick. Clouds absorb and reflect incoming solar radiation. Thus, the earth's surface is essentially deprived of significant short-wave (solar) input. The result is that the stratocumulus clouds substantially alter the surface energy budget. In addition, at the surface, the downward long wave radiation from low clouds effectively balances the outgoing long wave radiation from the surface. Lilly applied his original model over water. Under these circumstances, there is no diurnal variation in surface temperature.

Lilly theorized and then modeled an over water stratocumulus-capped convective boundary layer that was horizontally homogeneous, radiatively active, and turbulent. He assumed a strong "capping" inversion over a well mixed, nonprecipitating layer. For conservative variables, he used total moisture content ($q_w$) to account for the effects of water in a cloud ($q_w$ is the sum of the liquid water content of the air and the mixing ratio) and wet-bulb potential temperature ($\theta_w$) as a measure of latent and sensible heat content of the air. He further assumed that all the turbulence was generated as a result of cloud top evaporative cooling. A net outward radiative heat flux at the top of the well mixed layer dominates the turbulence flux generated by surface wind shear. Lilly hypothesized that the influence of shear-generated turbulence is negligible in a mixed layer of

thickness from 500 to greater than 1000 m.

## 2.2  Vertical Velocities in a Cloud-Topped Boundary Layer

The standard deviation ($\sigma$) of a variable is a measure of the spread of the data about its mean.  Vertical velocity variance ($\sigma_w^2$) is the square of the standard deviation, it is also a measure of the spread of observations about its mean

$$\sigma_w^2 = \frac{1}{N-1} \sum_{i=0}^{N-1} (w_i - \overline{w})^2. \tag{1}$$

However, by assuming a discrete definition of $\sigma_w^2$, vertical velocity variance will not include contributions from motions smaller than those that can be resolved directly.

For each data point (i), one can split a variable into its mean and turbulent parts ($w_i = \overline{w} + w'$), and rearrange the terms to solve for the turbulent part:  $w' = w_i - \overline{w}$. Substituting this into (1) yields

$$\sigma_w^2 = \frac{1}{N-1} \sum_{i=0}^{N-1} (w')^2. \tag{2}$$

If one assumes that N is large, such that $1/(N-1) \sim 1/N$, then

$$\sigma_w^2 = \frac{1}{N} \sum_{i=0}^{N-1} (w')^2. \tag{3}$$

An ensemble average is defined as

$$\overline{w}(t,s) = \frac{1}{N}\sum_{i=0}^{N-1} w_i(t,s),$$ (4)

where t = time and s = space. One can readily see the relationship between the vertical velocity variance ($\sigma_w^2$), and the turbulent part of vertical velocity (w'):

$$\sigma_w^2 = \overline{w'^2}.$$ (5)

Turbulence kinetic energy is derived from the equation of total kinetic energy per unit mass

$$KE/m = \frac{1}{2}(u^2 + v^2 + w^2).$$ (6)

One can partition the three velocity components (u, v, w) into mean and turbulent parts:

$$u = \overline{u} + u', \quad v = \overline{v} + v', \text{ and } w = \overline{w} + w'.$$ (7)

Substituting the mean and turbulent parts into the total kinetic energy equation (6), the turbulent kinetic energy per unit mass can be written as

$$TKE/m = \frac{1}{2}(\overline{u'^2} + \overline{v'^2} + \overline{w'^2}).$$ (8)

When one chooses the vertical component of TKE as an indication of the magnitude of turbulent kinetic energy, it

can be seen that vertical velocity variance is an important part of TKE (Lenschow et al., 1980):

$$2\,TKE/m = (\overline{u'^2} + \overline{v'^2} + \overline{w'^2}).$$ (9)

The scale of motion measurable by high temporal vertical velocity measurements is limited by the time interval between measurements. High temporal vertical velocity measurements from Doppler wind profilers represent the resolvable part of vertical motion. At least two measurements are required to resolve a wave. Two measurements with a time interval of 30 seconds can resolve motion variations on the order of 1 minute. Unresolvable motion, on a scale smaller than the time interval between measurements, is similar to subgrid-scale motions in an LES. The net field is calculated by summing the resolvable parts with the subgrid-scale parts. Similarly, large eddy simulation includes spatial averages such that turbulent eddies are broken into resolvable turbulence, in the energy containing range, and subgrid-scale terms. The resolvable scale turbulence can be calculated directly, while the subgrid-scale turbulence must be parameterized to reflect the transfer of energy from the resolvable scale to the subgrid-scale.

## 2.2.1  Vertical Velocity Variance Modeled in a Cloud-Topped Boundary Layer

Deardorff (1980) used a three-dimensional numerical model to study the turbulence structure of mixed layers capped by stratocumulus clouds. Seven cases were studied: Three having no liquid water phase changes and four including the effects of water phase changes. In all cases, a maximum in vertical velocity variance at height of about 40% of the depth of the boundary layer ($0.4\ z_i$), largely due to surface heating, was predicted. In the four cases where a phase change of liquid water was included, a secondary vertical velocity variance maximum between $0.9 \leq z/h \leq 1.1$ (where z is the height above the surface, and h is cloud top height) was evident. The peaks in vertical velocity variance at heights above $z/h = 1$ could be the result of internal wave motion within the strong capping inversion, or the result of truncation errors. The peaks below $z/h = 1$ were theorized to be the result of evaporative cooling of descending, entraining air in the region $0.95 \leq z/h \leq {\sim}1.05$. Albrecht et al. (1979) estimated that ~82% of cloud top radiative cooling occurs in the uppermost 5 mb (~50m) of clouds containing a mean liquid water content of $0.50\ g/m^3$. Moeng (1987) determined that 85% of the radiative cooling occurs in the entrainment zone at the top of the mixed layer.

Nicholls (1984) studied the structure of stratocumulus

clouds with aircraft observations. He also observed a secondary maximum of vertical velocity variance near cloud top. A temperature inversion above this level of increased variance tended to damp vertical motion and the variance was decreased.

Moeng (1986) later conducted large eddy simulations (LES) with stratus-topped boundary layers. The vertical velocity variance was shown to be dependent on the relative amount of cloud top cooling, and surface heating. The variance was decomposed into the sum of vertical velocity variance caused by cloud top radiative cooling plus the vertical velocity variance resulting from surface heating.

In this study, Moeng ran two simulations that included the interactions between turbulence and radiative cooling. Deardorff's (1980) subgrid-scale turbulence energy model, which included the effects of longwave radiation and condensation, was also included in Moeng's LES. To avoid decoupling of cloud and sub-cloud layers, short wave (solar) radiation was excluded. Simulation 1 included the effects of surface buoyancy flux; simulation 2 did not. Vertical velocity variance peaked at $z = 0.6 \ z_i$ in simulation 1, and at $z = 0.7 \ z_i$ in simulation 2. As a result of cloud top cooling, the total kinetic energy (the sum of vertical and horizontal contributions) in both simulations peaked at cloud top. Also, in both simulations, a secondary maximum in vertical velocity variance occurred at $z = 1.1 \ z_i$, possibly due to trapped

gravity waves in the overlying inversion. Table 2.1 summarizes the heights at which peaks in vertical velocity variance were determined.

Table 2.1: Summary of modeled vertical velocity variances.

| Modeler | Height of Variance Peak | Comments |
|---|---|---|
| Deardorff (1980) | $0.4\ z_i$ | With and without liquid water phase change. |
| | $0.9\ z_i \leq z_i \leq 1.1\ z_i$ | With liquid water phase change. |
| Nicholls (1984) | $1.0\ z_i$ | In-cloud. |
| | $0.3\ z_i$ | Sub-cloud. |
| Moeng (1986) | $1.1\ z_i$ | Simulation 1 & 2 |
| | $0.6\ z_i$ | Simulation 1 (with surface heating) |
| | $0.7\ z_i$ | Simulation 2 (no surface heating) |

## 2.2.2 Vertical Velocity Variance in a Cloud-Topped Boundary Layer Over Land

Convective boundary layers topped by stratocumulus clouds also commonly occur over land (Astling, 1976; Caughey et al., 1982; Roach et al., 1982; Slingo et al., 1982; Caughey and Kitchen, 1984). But there are only a few studies of these cloud-topped atmospheric boundary layers over land. Nevertheless, land-based stratocumulus studies have the potential of substantially increasing our understanding of cloud-topped atmospheric boundary layers.

Astling (1976) numerically modeled low level cloud formation in the cold air region to the west of a continental United States cyclone. In the absence of significant surface heating and secondary upper-level dynamics, surface frictional stress was determined to be the primary cause of low-level stratocumulus formation to the west of the cyclone center.

Caughey et al. (1982) studied the small-scale air motion of nocturnal stratocumulus. In nocturnal stratocumulus, turbulence is driven by buoyancy fluctuations near cloud top as a result of cloud top radiative cooling. The characteristic length scale of the vertical velocity fluctuations within the cloud layer is estimated to be about 30 m. This horizontal scale relates to the vertical distance over which the majority of radiative cooling occurs near cloud top.

The vertical velocity variance ($\sigma_w^2$) was nearly uniform in the cloud layer (Caughey et al., 1982). However, when $\sigma_w^2$ was scaled with the depth of the cloud layer (d), a slight maximum was observed at half the depth of the cloud layer. Above cloud top, $\sigma_w^2$ decreased markedly; an indication that turbulence probably ceases above the entrainment interfacial layer (EIL). The base of the EIL is defined by the inversion base, and the upper boundary is the height above the inversion base at which the vertical velocity variance decreases. Caughey and Kitchen (1984) also studied the turbulent structure of nocturnal stratocumulus clouds. Typical values

of the vertical velocity variance dropped by an order of magnitude across cloud top. However, their data do not substantiate a $\sigma_w^2$ maximum at half the cloud depth. Instead, their data suggests that the height of the boundary layer ($z_i$) is the applicable length scale, and a weak maximum exists at $z/z_i = 0.80 - 0.85$. The variation in the maximum vertical velocity variance ($\sigma_{w(max)}^2$) can be related to the rate of cloud top cooling. In case study 1, $\sigma_{w(max)}^2$ was ~5 $m^2/s^2$ with a maximum cloud top cooling rate of ~8°K/hr. Case study 2 noted $\sigma_{w(max)}^2$ was ~2 $m^2/s^2$ with a cooling rate of ~5 °K/hr.

Chapter 3

INSTRUMENTATION


Most of the data presented in this thesis were obtained using two of Penn State's UHF wind profilers. High temporal resolution vertical velocity and reflectivity measurements from them were used to identify the vertical structure of a cloud-topped atmospheric boundary layer over land.


## 3.1  Clear Air Doppler Wind Profilers


A direct means of measuring vertical motions with a wind profiler is to use the zenith (vertical) beam. The zenith measurement of Doppler radial velocity ($V_r$) is, in principle, a straightforward measure of vertical wind velocity. A typical configuration for wind profilers is use of three beams. One beam is pointed vertically to measure the vertical wind velocity, the other two are usually oriented 90° apart in azimuth, and about 15° off zenith. The off-zenith beams are used to calculate horizontal wind components. In addition, the off-zenith beams can also be used to calculate vertical winds from the vector radial wind measurements.

The radial velocity of a target is determined by the amount of frequency change between the radio frequency source (radar emitter), and the target-scattered radiation. This difference is the Doppler shift. Its magnitude is

proportional to the relative radial velocity between the source and the target. The Doppler frequency for a back scattered signal

$$f_d = -\frac{2v_r}{\lambda},$$ (10)

is proportional to the relative radial velocity ($v_r$) of the scatters, and inversely proportional to the transmitted wavelength ($\lambda$). The factor of two is the result of the increasing path travelled by the radar signal, i.e., to and from the target. The negative sign is a convention that relates motion away from the radar as a negative value, and that towards the radar source as positive.

The ability of wind profilers to detect air motion depends on the variations in the radio index of refraction. Turbulent eddies in the atmosphere produce temperature and moisture inhomogeneities over relatively short distances. These irregularities prove to be good tracers of the mean wind. Variations in the air properties can be transformed into variations of the radio index of refraction (Bean and Dutton, 1966). In short, the atmospheric radio index of refraction is a measure of the rate at which radio waves propagate through the atmosphere, and is a function of pressure, temperature, and moisture content of the atmosphere.

The refractive index (n) is defined as the ratio of the speed of light in a vacuum (c) to the speed of an electromagnetic wave (v) in a medium (in this case . . . air)

$$n = \frac{c}{v} . \tag{11}$$

In the atmosphere n is very nearly unity, a more useful value of the index of refraction is the radio refractivity (N). It is

$$N = (n-1) \times 10^6 . \tag{12}$$

A typical value for n at sea level is 1.0003, the corresponding N-value is 300.

To account for the differences in pressure, temperature, and moisture in the atmosphere, the moist radio refractivity (N) can be calculated from

$$N = 77.6 \frac{p}{T} - 5.6 \frac{e}{T} + 3.75 \times 10^5 \frac{e}{T^2} , \tag{13}$$

where p is the atmospheric pressure (mb), T is the temperature (K), and e is the vapor pressure (mb). At the surface (1013 mb), a typical temperature is 288 K, and a typical vapor pressure is 10.2 mb (Bean and Dutton, 1966). The second term on the right-hand-side of (13) can be neglected. It is typically less than 0.1% of the total index of refraction (N). As a consequence, a more commonly used form of (17) is

$$N = \frac{77.6}{T} (p + 4810 \frac{e}{T}) . \tag{14}$$

Variations in the index of refraction are related to the radar signal return through the structure function parameter

of the refractive index $(C_n^2)$. The structure function parameter is a measure of the mean-square fluctuation of the refractive index as a function of distance. The structure function of refractive index

$$D_{nn}(R) = \frac{1}{N}\sum_{k=0}^{N-1} [n_k - n_{k+j}]^2, \qquad (15)$$

is the mean square difference in two points between a spatial series having a separation of R, where R = j ΔR. Similarity theory suggests (Stull, 1988) that

$$D_{nn}(R) = C_{n^2}R^{\frac{2}{3}}. \qquad (16)$$

For isotropic turbulence in the inertial subrange, radar reflectivity (η) for volume scattered distributed targets is (Ottersten, 1969)

$$\eta = 0.38\ C_{n^2}\ \lambda^{-\frac{1}{3}}, \qquad (17)$$

where λ is the wavelength of the radar.

The radar equation for distributed targets is given by

$$P_r = \frac{P_t A_e \pi a^2 \Delta r L}{64 r^2}\eta, \qquad (18)$$

where $P_r$ is the average received power for an isotropic volume scatter, $P_t$ is the transmitted power, $A_e$ is the effective antenna area, a is an antenna efficiency which accounts for non-uniform antenna illumination, and L is an attenuation factor associated with antenna and transmission line losses.

The depth of the scattering volume (range gate width) is $\Delta r$, and r is the distance to the center of the scattering volume. One can combine equations 17 and 18 to give:

$$P_r = \frac{P_t A_e \pi a^2 \Delta r L}{168.4 f^2 \lambda^{1/3}} C_{n^2}.$$ (19)

The ratio of received power $(P_r)$ to accompanying background noise $(P_n)$ is defined as the signal-to-noise ratio (SNR)

$$SNR = P_r/P_n.$$ (20)

The signal-to-noise ratio is generally used in radar meteorology to define that amount of atmospheric signal discernable above a background noise, and it can be related to radar reflectivity by (VanZandt et al., 1978)

$$\eta = \frac{9\pi}{2} \frac{ckB(T_c + T_{rx}/\alpha)}{\alpha P_t F_r A_e Cos(\chi)} \left(\frac{r}{\Delta r}\right)^2 (SNR).$$ (21)

Here, c is the speed of light in a vacuum, k is Boltzman's constant, and B is the bandwidth of the signal processing integrating filter, the pulse repetition frequency divided by the number of spectra averaged $(F_r/n)$. The radar transmission line efficiency is $\alpha$. Cos $(\chi)$ accounts for the apparent reduction of the antenna area when it is viewed at an oblique angle. One can see that its value is 1.0 in the vertical ($\chi$ = 0). When measuring horizontal winds with a 15° off-zenith wind profiler, the received power of a collinear-coaxial

antenna is reduced by 3% (cos 15° ~ 0.97). One can combine equations (17), (19), and (20) to yield an equation relating the average received power to the signal-to-noise ratio through the index of refraction structure function parameter, and specific radar characteristics:

$$Pr \propto (\text{Radar Characteristics})(\text{SNR}). \qquad (22)$$

## 3.2 Instrument Limitations

Although there have been many advances in atmospheric remote sensing and signal processing, caution is still necessary to ensure that profiler data is properly interpreted. For example, proper antenna geometry is absolutely critical for measurements of vertical air motions. An angular offset in the vertical beam of a wind profiler can produce significant measurement errors in the presence of strong horizontal winds. Horizontal homogeneity is assumed in the measurement volume. Radar beam dimensions and operating characteristics may also limit the profiler resolution. Vertical range (a function of radar output power and received power) and vertical resolution (a function of radar pulse width) are both limiting factors to profiler resolution. In addition, precipitation fall velocities can contaminate "clear-air" data. Sources of error such as these must be identified and removed before unambiguous and accurate "clear-

air" measurements can be used for model validation purposes.

## 3.2.1  Horizontal Wind Contamination

Typical synoptic scale vertical motions in atmospheric cyclones are on the order of 5-10 cm/s.  The magnitude of atmospheric horizontal winds is substantially larger than is that of the vertical motions.  The ratio of mean horizontal to vertical winds, in the synoptic scale, is on the order of $10^2$ (m/s vs. cm/s).  Such synoptic scale disturbances typically have spatial scales of 1500-2000 km, and life cycles of 3-7 days.  Frontal zone series may have a typical life span of 1 month.   As a result of these large time scales, vertical velocity (w) time averages greater than 1 month are necessary to remove time dependent bias errors associated with the measurement of vertical velocities over synoptic cycles. Remaining errors will often then reflect an instrument bias in the measurement system.

A bias in zenith antenna angle can cause a substantial bias in the measurement of the vertical velocities as a consequence of strong horizontal winds.  The 3-dimensional geometry of the zenith antenna bias can be broken into vertical and horizontal components (figure 3.1).  The bias angle (the error angle) in the zenith direction is $\phi$, and as a consequence of $\phi$, $\gamma$ is the corresponding bias angle in the horizontal (x-y) plane.  If $\phi=0$, then no horizontal wind will

$V_r \sin(\phi) = V_h \cos(\gamma - \theta)$

$w_t = V_r \cos(\phi)$

$\phi$

$V_r = w_t \cos(\phi) + V_h \cos(\gamma - \theta) \sin(\phi)$

$\theta$

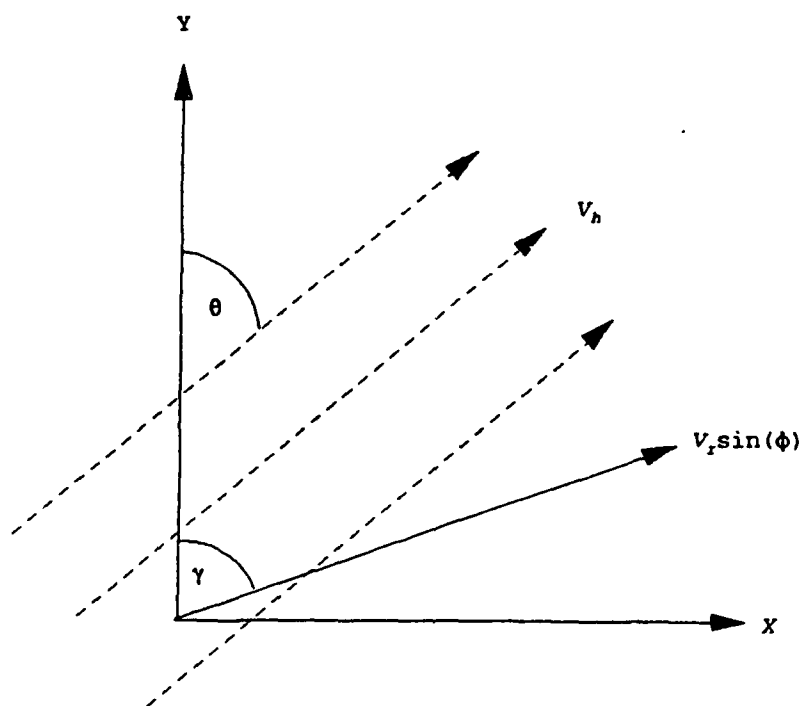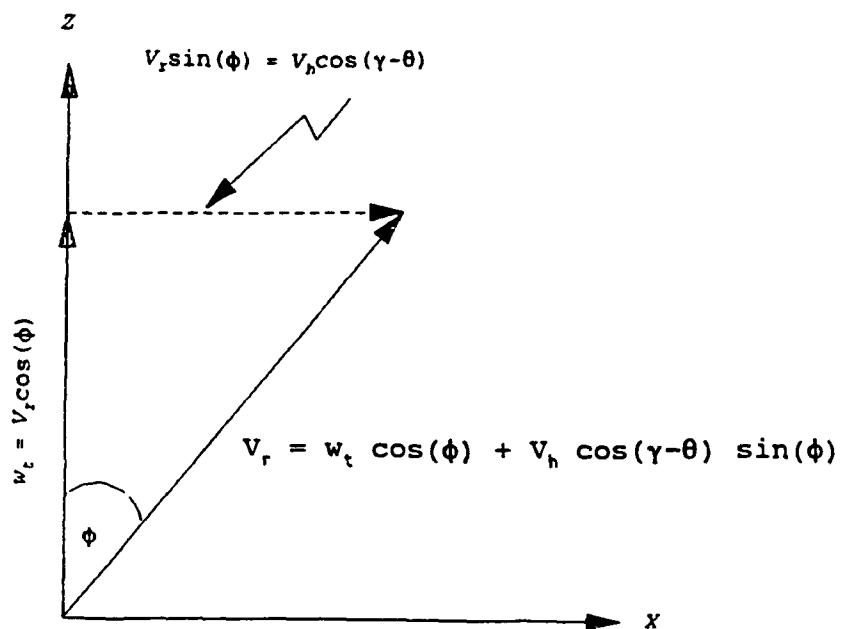$V_h$

$V_r \sin(\phi)$

$\gamma$

Figure 3.1   3-D geometry of zenith beam bias angles.   Top: vertical cross-section.   Bottom:   horizontal cross-section.

be reflected in the zenith direction. The direction of the horizontal wind is denoted as $\theta$. The measured radial velocity $(V_r)$ can be described using the sum of the true vertical velocity $(w_t)$ and horizontal winds $(V_h)$ with respect to the bias and prevailing wind directions. The resulting equation

$$V_r = w_t\cos(\phi) + V_h\cos(\gamma-\theta)\sin(\phi) \qquad (23)$$

is a single equation with 2 unknowns, $\gamma$ and $\phi$ ($w_t$ is a function of $\gamma$ and $\phi$).

One can assess the sensitivity of $V_r$ to each of its components by taking the total derivative of (23) to give

$$dV_r = [V_h\cos(\gamma-\theta)\cos(\phi) - w\sin(\theta)]\,d\phi + [\cos(\phi)]\,dw_t$$

$$+ [\cos(\gamma-\theta)\sin(\phi)]\,dV_h - [V_h\sin(\gamma-\theta)\sin(\phi)]\,d(\gamma-\theta). \qquad (24)$$

Using representative values of $w_t = 0.05$ m/s, $\phi = 0.25°$, $V_h = 5$ m/s, and $(\gamma-\theta) = 0$ (to produce the maximum effect due to horizontal wind) yields

$$dV_r = 0.99999\,dw_t + 4.99973\,d\phi + 0.00436\,dV_h. \qquad (25)$$

If one assumes $dw_t \sim 0.2$ m/s, $d\phi \sim 0.05°$, and $dV_h \sim 5$ m/s the contributions of each component to the change in $V_r$ is 42% for $w_t$, 53% for $\phi$, and 5% for $V_h$. This indicates that the radial velocity $(V_r)$ is primarily sensitive to the bias angle $(\phi)$ and the true vertical velocity $(w_t)$. Only a small contribution is from $V_h$. Thus, precise and accurate zenith

beam orientation is critical to insure proper measurement of atmospheric vertical velocities.

For any given zenith error angle ($\phi$), there are a number of horizontal error angles that can give $\cos(\gamma-\theta)\sin(\theta)$ a constant value. The problem is to determine the most probable values of $\gamma$ and $\phi$ that will result in a biased $V_r$. Post-processing of radial velocity measurements, with angular biases removed, will yield unbiased vertical velocity measurements.

It is necessary to identify measurement errors in order to remove them. Random and systematic errors are two general types of errors that occur in all measurements. A random error can occur in either direction about a mean value, and may have differing magnitudes. The variance of an estimate ($Var[\hat{\phi}]$) is a random error associated with the expected value of the difference between the mean value and the true value, squared

$$Var[\hat{\phi}] = E[(\hat{\phi}-E[\hat{\phi}])^2].$$

(26)

The other type of error, systematic error, is the difference between the expected value of an estimate ($E[\hat{\phi}]$) and the true value $\phi$. In a repeatable measurement, the bias of an estimate ($b[\hat{\phi}]$) is a systematic error, which unlike a random error, always occurs in the same direction and with similar magnitude.

The mean square error ($E[(\hat{\phi}-\phi)^2]$) is defined as the

expected value of the squared quantity of the deviation from the estimate. In other words, the mean square error is the sum of the variance and the square of the bias

$$E[(\hat{\phi}-\phi)^2] = Var[\hat{\phi}] + [b[\hat{\phi}]]^2. \tag{27}$$

Figure 3.2 exemplifies the difference between biased estimators of random data and unbiased estimators with differing variances. Curves a and b are all centered about $\theta$. The peak of this probability density function ($p\{\theta\}$) represents the expected value of $\theta$ ($E\{\theta\}$). Since a and b are centered on $\theta$, the true value of $\theta$ ($E\{\theta\} = \theta$) is an unbiased probability density function. Curve b shows a larger degree of variance than curve a. However, curve a has extreme deviations more frequently than curve b.

Curve c shows the least amount of variance, but it is not centered about $\theta$. It is biased by the amount $E\{\theta\} - \theta$. Curve c is also the best estimate of $\theta$ because of its small variance; however, its desirability is decreased because the average of the biased estimates will always be biased too. The average of the unbiased estimates will always be unbiased.

Averages of wind profiler data over long periods of time will nearly eliminate the random measurement errors. Given the scale of synoptic scale meteorological systems, three months of hourly data appear to be sufficient to identify biases and eliminate random errors.

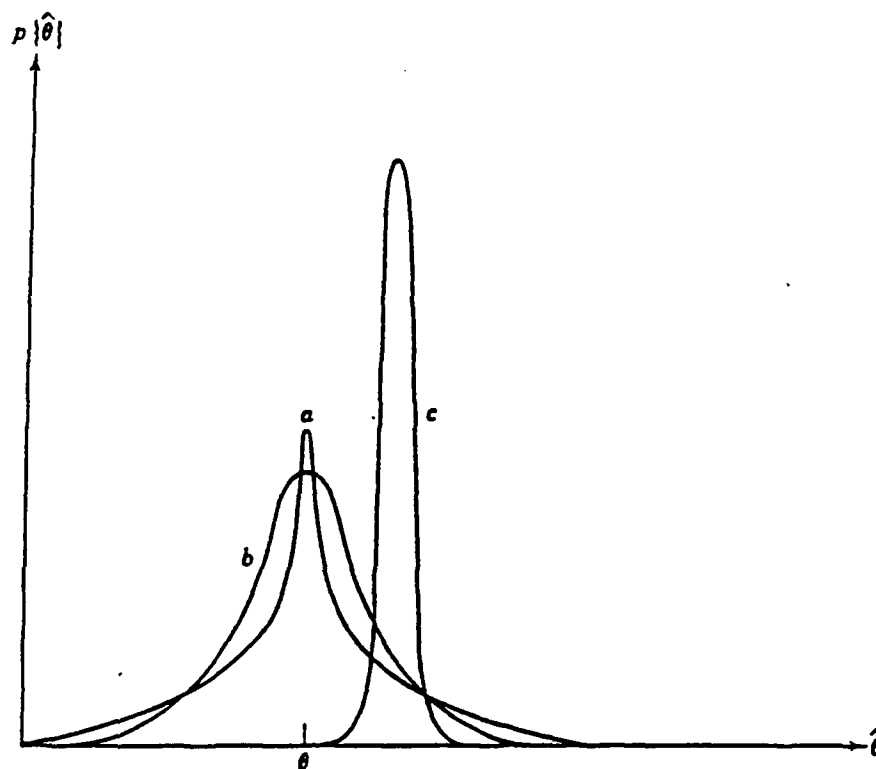A source of bias in the vertical beam of a Doppler wind

Figure 3.2  Example of biased and unbiased estimators of
random data with differing variances (Source:
Brownlee, 1965)

profiler is due to the contributions of other inputs which are correlated with the measured input. In equation (23), the measured parameter is $V_r$. This radial velocity represents the biased zenith beam intending to measure the true vertical velocity ($w_t$). It is biased by the contribution of the horizontal wind ($V_h$) and the associated error angles ($\gamma$ and $\phi$). If the angles $\gamma$ and $\phi$ can be determined for each wind profiler system, the bias of the measurement can be subtracted from the measured radial velocity to yield the true vertical velocity.

The apparent bias in the vertical beam may be the result of a number of factors. At least four possibilities exist which can help to explain the bias problem. First, if the antenna is physically not level, a bias can occur. A typical 915 MHz antenna has dimensions on the order of 1 X 3 meters. A rise of only 1.3 cm along the 3 meter length of the antenna can induce a bias error ($\phi$) of 0.25°. This will add a horizontal velocity error of 0.4% of the horizontal wind. A 404 MHz antenna, approximately 6.5 m on a side, will only need a 2.8 cm rise to induce a 0.25° zenith error. For example, with a 10 m/s horizontal wind, and a bias angle of 0.25°, the contribution to the radial velocity is 0.04 m/s (4 cm/s). Given a typical vertical velocity of 5-10 cm/s, a 44% to 88% error has been introduced. Clearly, an error in excess of 100% is not only possible, it is probable.

Another possibility for a bias angle error is that

associated with a standing wave which could persist over the radar (Barry and Chorley, 1982). One might argue that since an atmospheric standing wave is a synoptic feature dependent on the prevailing atmospheric conditions and orographic effects, it would be random error that should be averaged out over a long period of time. However, orographically induced standing waves may persist under a variety of synoptic conditions. Their persistence may exceed the time needed to average out synoptic scale features.

A third possibility for a bias error may be the result of a non-ideal radar antenna patterns. Ideal beam patterns reflect energy distributed symmetrically around the beam axis. An asymmetrical beam may well reflect energy biased, or weighted, towards the uneven portion of an asymmetrical beam.

A fourth possibility for a bias may be with the signal processing (FFT) routine. Clutter suppression techniques used on wind profilers may bias measurements. Zero suppression filtering is one such clutter suppression technique. Zero suppression "clips" the spectral peak at the zero FFT bin as well as N user-prescribed bins on either side. This forces the algorithm which picks the spectral peaks to choose values outside the range of clipped values. Post-processing will not provide unbiased measurements.

With a very long time scale to remove time-dependent bias errors, and a permanent antenna foundation, the cause of the antenna bias (electrical or physical) should not be as

important as the amount and direction of the vertical velocity bias. Once the apparent angular bias has been determined, the bias can be removed from measured vertical velocities, and its cause should be of secondary importance.

## 3.2.2  Precipitation Contamination

For Rayleigh scatterers, radar reflectivity ($\eta$) varies as

$$\eta \sim \frac{|K|^2}{\lambda^4} \sum_i D_i^6, \tag{28}$$

where $|K|^2$ is a dielectric factor, $\lambda$ is the radar wavelength, and $D_i$ is the diameter of the individual scatters in the measurement volume (Battan, 1973). Large diameter precipitation, for a given concentration, will produce greater reflectivities than small drops. Also, since the reflectivity for hydrometeors varies as $\lambda^{-4}$, one would expect higher frequency radars (shorter wavelengths) to be more sensitive to precipitation than lower frequency radars (longer wavelengths).

Recall that reflectivity for clear air varies as $\lambda^{-1/3}$. Precipitation sensitive radars (S-band for example) are less sensitive to clear air refractive index variations than UHF radars. Conversely, UHF radars are less sensitive to precipitation than S-band radars. However, within the UHF band (300 Hz to 3000 Hz), higher frequency profiling radars are more sensitive to precipitation than are the lower

frequency systems. In a comparison between 915 MHz and 404 MHz profilers, one would expect a higher sensitivity to precipitation with the 915 MHz profiler.

When one is interested in the vertical motion of air, precipitation can be a problem. The vertical motion detected by the radar may well be the precipitation fall velocity and not the clear vertical air motion. In the presence of precipitation, a filter must be employed to remove precipitation fall velocity from the clear air motions.

### 3.2.3  Data Sampling and Filtering

The wind profiler data used for this thesis were averaged over one-hour periods. Measurements every 30 seconds yielded 120 unfiltered samples per hour. This quantity proved to be sufficient to produce meaningful statistics for lower-level, hourly-averaged, profiler data. Problems arose during transition from cloudy convective boundary layers to clear skies. As the sky cleared, fewer and fewer cloud statistics were available. Hourly averages of only a few data may not produce statistically significant data of the mean cloud-topped atmosphere.

As a result of data processing, weak signals may eliminate some data. Environmental and atmospheric noise has a large contribution to wind profiler signal because of the profiler's relatively low frequency. Antenna design, radar

location, and frequency all define the system noise (Keeler et al., 1990). The Signal-to-Noise Ratio (SNR) cut-off for Penn State's wind profilers were determined by previous use and adjustment. The cut-off for SNR for the 915 MHz profiler was -10 db, the 404 MHz profiler used -15 db. Any signal less than the prescribed value was considered questionable relative to the background noise. SNR filtering eliminates a great deal of questionable data.

Vertical resolution of the wind profilers is a function of the length of the transmitted pulse,

$$RESOLUTION = c(\tau/2). \tag{29}$$

Where c is the speed of light (m/s), and $\tau$ is the length of the transmitted pulse ($s^{-1}$). Typical axial resolution for UHF wind profilers is 100 m to 300 m. For thin cloud layers, profiler resolution may be too coarse to produce meaningful statistics. Stratocumulus cloud thicknesses of less than 500 m are quite commonly observed (Albrecht et al., 1985; Rogers and Yau, 1989).

Chapter 4

MEASUREMENTS

## 4.1   Boundary Layer Data

Data were gathered on 20 March 1991, and 31 January 1992. On both dates, post-cold-frontal stratocumulus covered the area.

### 4.1.1   20 March 1991 Data

To measure mean wind and temperature profiles, radiosondes were launched on 20 March 1991, from the roof of Penn State's Walker building.  Potential temperature gradient was used to establish the top of the well-mixed layer.  Cloud base was determined by a laser ceilometer sited on the roof of the Walker building.  Both the 915 MHz and 404 MHz wind profilers were operated at the nearby Circleville Farm site. The profilers were programmed to measure velocities in the boundary layer in the vertical mode only.  For high temporal resolution, data were sampled in 30 second intervals.  Initial analysis of the data indicated that there was a probability of a bias in the vertical beam of the 915 MHz profiler.  To verify a horizontal wind contamination, or other bias, it was decided that horizontal wind information from the 404 MHz profiler would yield high temporal resolution data at range gates comparable to the 915 MHz profiler.

Three radiosondes were launched from the roof of the

Walker building on 20 March 1991. The first (designated launch A) was launched at 1423 Z. The second (launch B) was at 1335 Z, and the third (launch C) at 2000 Z. Ceilometer data were gathered every 30 seconds, also from the Walker Building. Cloud cover was decreasing during this period indicating that the boundary layer was in transition from a cloudy convective boundary layer to a clear convective boundary layer. Figure 4.1 depicts the ceilometer data. One can easily see that the boundary layer was in transition. The boundary layer thickness increased as the hourly cloud cover decreased. Figure 4.2 overlays the three radiosonde profiles of potential temperature. In all three cases, potential temperature remained relatively constant with height up to the inversion base, indicating that the layer was well mixed. Potential temperature increased from 1423 Z to 2000 Z indicating an increase in solar energy input, and surface heating. Also, figure 4.2 indicates that the well mixed layer increased its thickness with time. Figure 4.3 depicts the mixing ratio profile for 20 March 1991. Cloud top is indicated by a sudden decrease in mixing ratio with height.

Table 4.1 summarizes the combined radiosonde/ceilometer data. Cloud cover decreased from 74% to 4% over this 5 1/2 hour period indicating a transition from a cloudy convective boundary layer to a clear convective boundary layer. Note that the cloud thickness also decreased with time, and in the clear sky case (launch C), the Lifting Condensation Level

STATE COLLEGE, PA  20 MARCH 1991
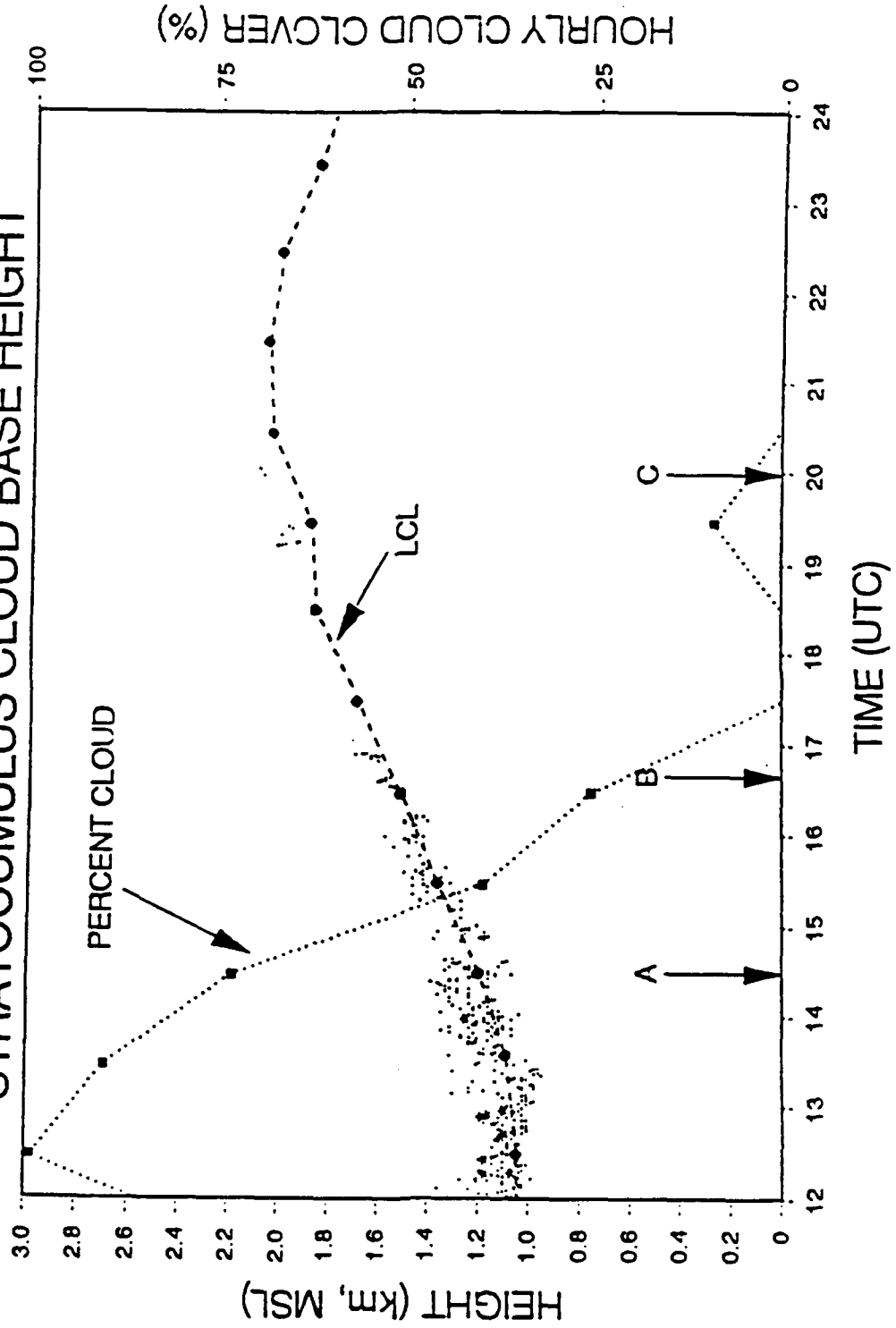STRATOCUMULUS CLOUD BASE HEIGHT

HOURLY CLOUD CLOVER (%)

HEIGHT (km, MSL)

TIME (UTC)

PERCENT CLOUD

LCL

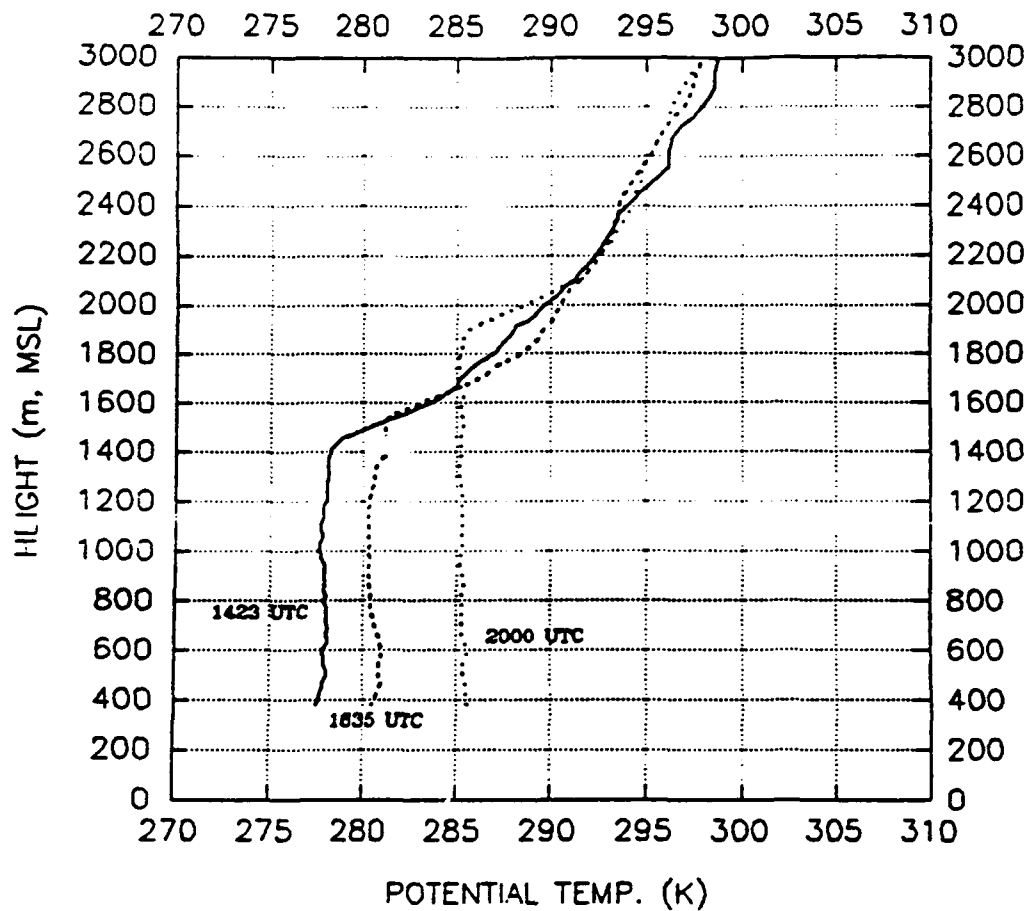A    B    C

Figure 4.1  Cellometer data for 20 March 1991

Figure 4.2 Potential temperature profiles for 20 March 1991
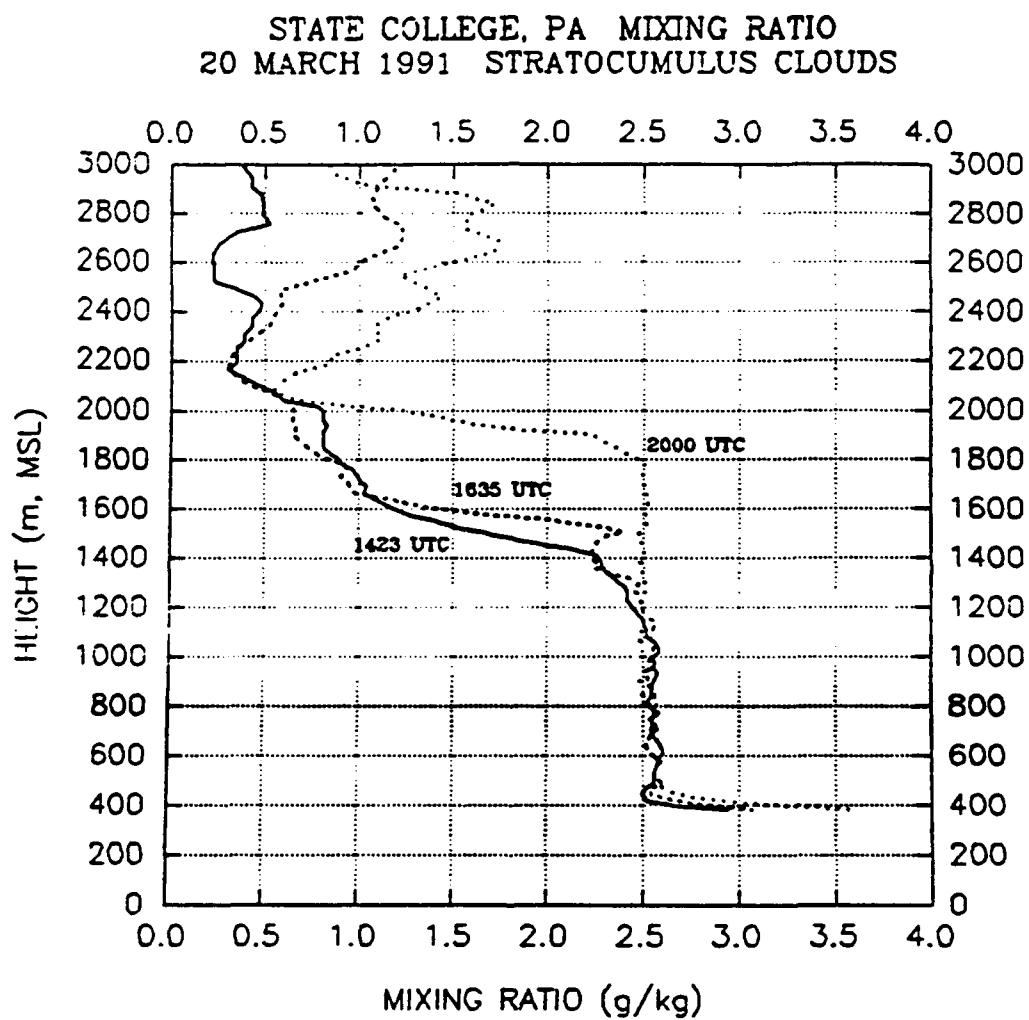
Figure 4.3   Mixing ratio profiles for 20 March 1991

(LCL) was higher than the top of the mixed layer.

Table 4.1: Summary of radiosonde and ceilometer measurements for 20 March 1991.

| Sonde | Time(Z) | % Cloud | Cloud Base(MSL) (LCL) | Cloud Top(MSL) | Cloud Thickness(M) |
|-------|---------|---------|-----------------------|----------------|--------------------|
| A | 1423 | 74 | 1200 | 1450 | 250 |
| B | 1635 | 23 | 1510 | 1550 | 40 |
| C | 2000 | 4 | 1950 | 1900 | --- |

## 4.1.2   31 January 1992 Data

Data collected on 31 January 1992 also included high temporal resolution 915 MHz vertical velocities. The 404 MHz profiler was programmed to include horizontal wind measurements at each level. Horizontal winds from the 404 MHz profiler were used to determine the possibility of, and extent of horizontal wind contamination to the 915 MHz vertical velocities. The trade-off was that the 404 MHz profiler yielded fewer vertical measurements than the 915 MHz profiler for the same time period. However, once a determination was made that a bias in the vertical beam of the 915 MHz profiler existed, a return to the high temporal resolution 404 MHz data from 20 March 1991 yielded some clues into the structure of the cloud-topped atmospheric boundary layer, at least insofar as it can be derived using a clear-air Doppler radar.

No radiosondes were available for the 31 January data

set. As a result, and unfortunately, no boundary layer thermodynamic variables were available. The laser ceilometer was used for determining cloud base height. Also, Penn State's new 94 GHz cloud radar was available and sufficiently operational to determine cloud top height. However, the 94 GHz cloud radar was not yet functional in the Doppler mode. At least high temporal resolution cloud top height could be determined. Figure 4.4 overlays the ceilometer and 94 GHz data. Using the two instruments, the stratocumulus deck was clearly depicted.

Table 4.2 summarizes cloud base and top height statistics for each hourly average. Clearly evident from figure 4.4 and table 4.2 is the increased scatter in the cloud base as a result of precipitation. The standard deviation ($\sigma$) of cloud top doesn't reflect the precipitation at the base of the cloud. Also, cloud thickness increases as the mean height of the cloud base decreases from the precipitation.

Table 4.2: Summary of 94 GHz cloud radar and ceilometer measurements for 31 January 1992.

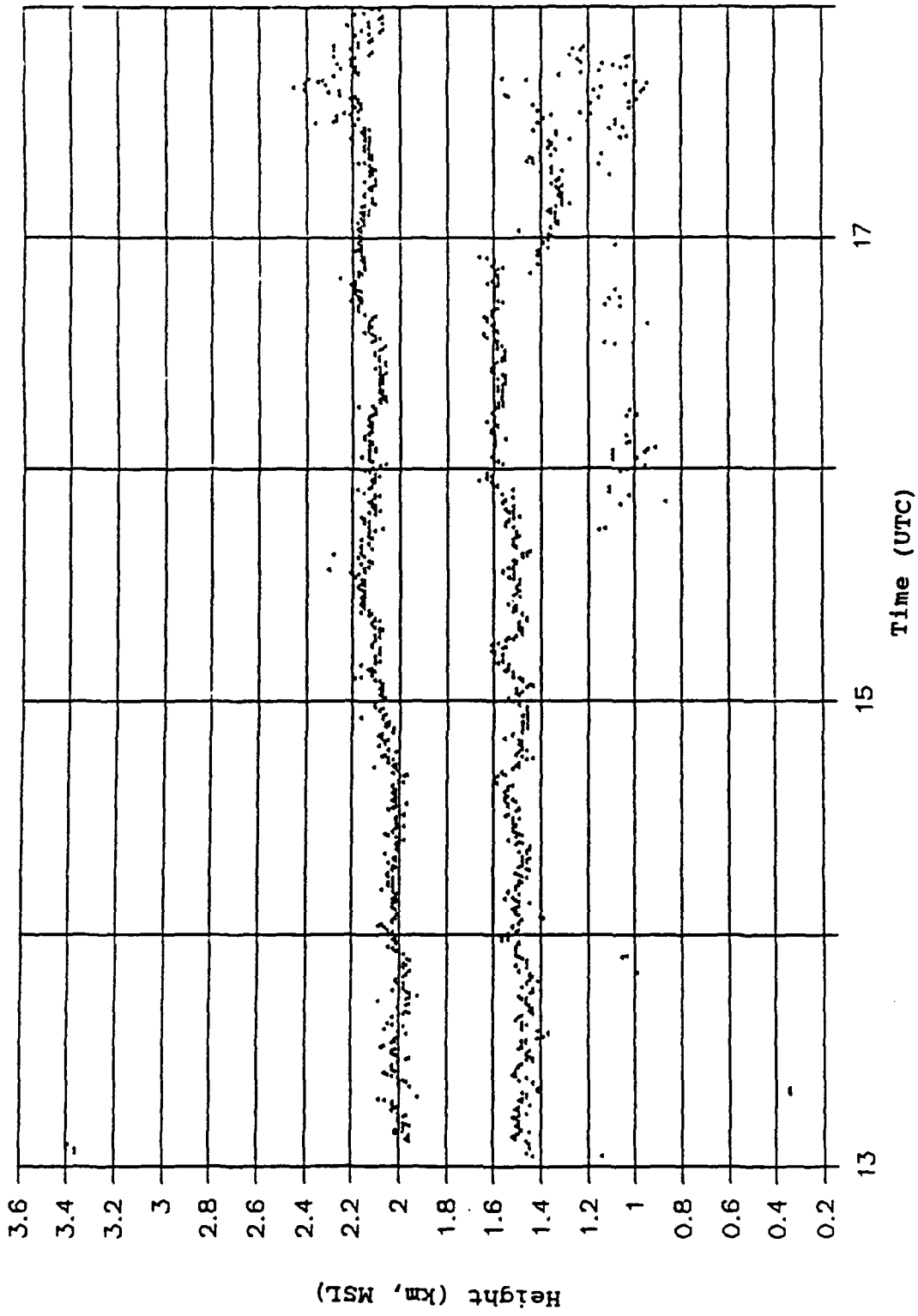| Cloud Top Statistics (94 GHz) | | | Cloud Base Statistics (Ceilometer) | | | |
|---|---|---|---|---|---|---|
| Hour (Z) | Height (M) Avg (MSL) | $\sigma$ | Hour (Z) | Height (M) Avg (MSL) | $\sigma$ | Cloud Thickness (M) |
| 13 | 1962 | 438 | 13 | 1502 | 36 | 460 |
| 14 | 2036 | 31 | 14 | 1531 | 38 | 505 |
| 15 | 2158 | 38 | 15 | 1517 | 122 | 641 |
| 16 | 2135 | 169 | 16 | 1514 | 223 | 621 |
| 17 | 2207 | 72 | 17 | 1322 | 154 | 885 |

Figure 4.4  Combined ceilometer and 94 GHz cloud radar time series indicating cloud base and top for 31 January 1992

## 4.2   Data Processing and Filtering

For high temporal resolution, the vertical wind profiler data were recorded in 30 second intervals. In this mode, one 24-hour period of formatted wind data filled ASCII files in excess of 5.8 Mbytes. All data were processed on a 386 PC. As a result of the large file sizes, they had to be broken into hourly segments for analysis. Hourly, filtered data files of 30 second vertical velocity and SNR data were about 150 Kbytes in length. Initial filtering consisted of Signal-to-Noise filtering to eliminate data which were questionable relative to the background noise. Another filter was an arbitrary filter based on anticipated vertical velocity values. A low flying aircraft or signal from precipitation fall velocity could, and did occasionally, contaminate the "clear-air" vertical velocity profiles. An initial cut off of ±2 m/s was used to eliminate potential contamination from such sources. Subsequent further analysis indicated a ±1 m/s cut-off was more appropriate for the precipitation sensitive 915 MHz profiler.

## 4.2.1   SNR Filtering

One-hour data blocks were extracted from the 24-hour file and filtering was performed. Data from the 915 MHz profiler with SNR values less than -10 db (-15 db for the 404 MHz

profiler) were deemed too weak to be discernable from background noise and were omitted from further statistical analysis.


## 4.2.2  Precipitation Filtering


Another filter used on the raw vertical velocity data was a precipitation/aircraft filter.  This filter was employed after the fact.  Figure 4.4 depicts a time series of ceilometer cloud base and 94 GHz cloud top.  Increased variance and decreased cloud base indicate that the cloud started precipitating beginning just prior to 1600 Z.  Figures 4.5 through 4.9 represent time series of vertical velocities for the 915 MHz profiler at selected heights from 17:00:00 Z to 17:59:30 Z, 31 January 1992.  Below cloud base (figure 4.5), a relatively tight series of vertical velocities exist in the vicinity of 0 ± ~0.1 m/s.  This is what one would expect in typical clear air vertical velocities.  A second series of vertical velocities appear during the second half of the hour with magnitudes of nearly 2 m/s.  The nearest sounding available for this period is a 12 Z Pittsburgh radiosonde.  The freezing level for the Pittsburgh sounding is approximately 950 m (AGL).  The 915 MHz time series indicate downward velocities of up to 2 m/s.  Although there is insufficient information to accurately determine the type of precipitation, one would deduce from the height of the
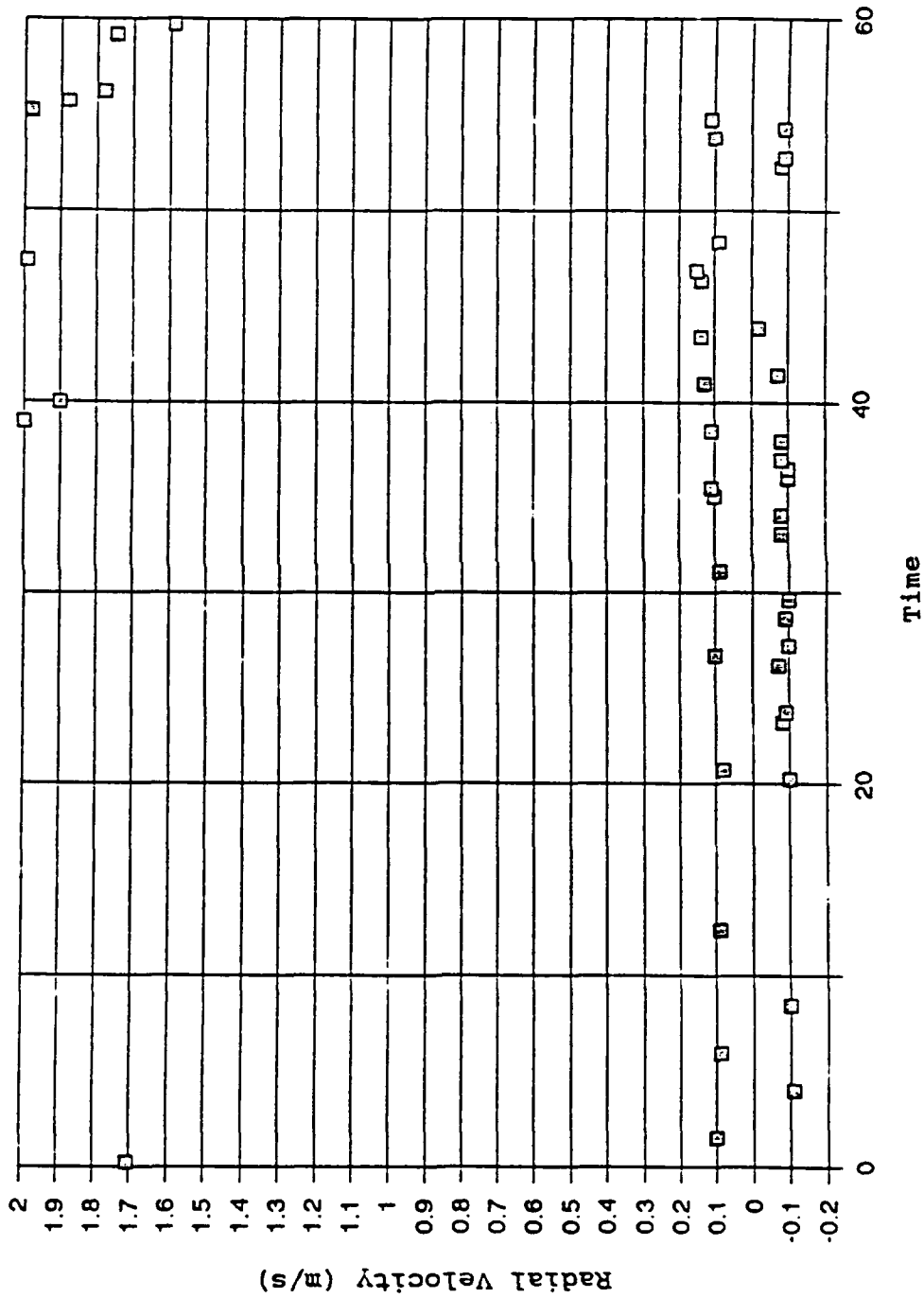
Figure 4.5  Time series of radial velocities from the 915 MHz
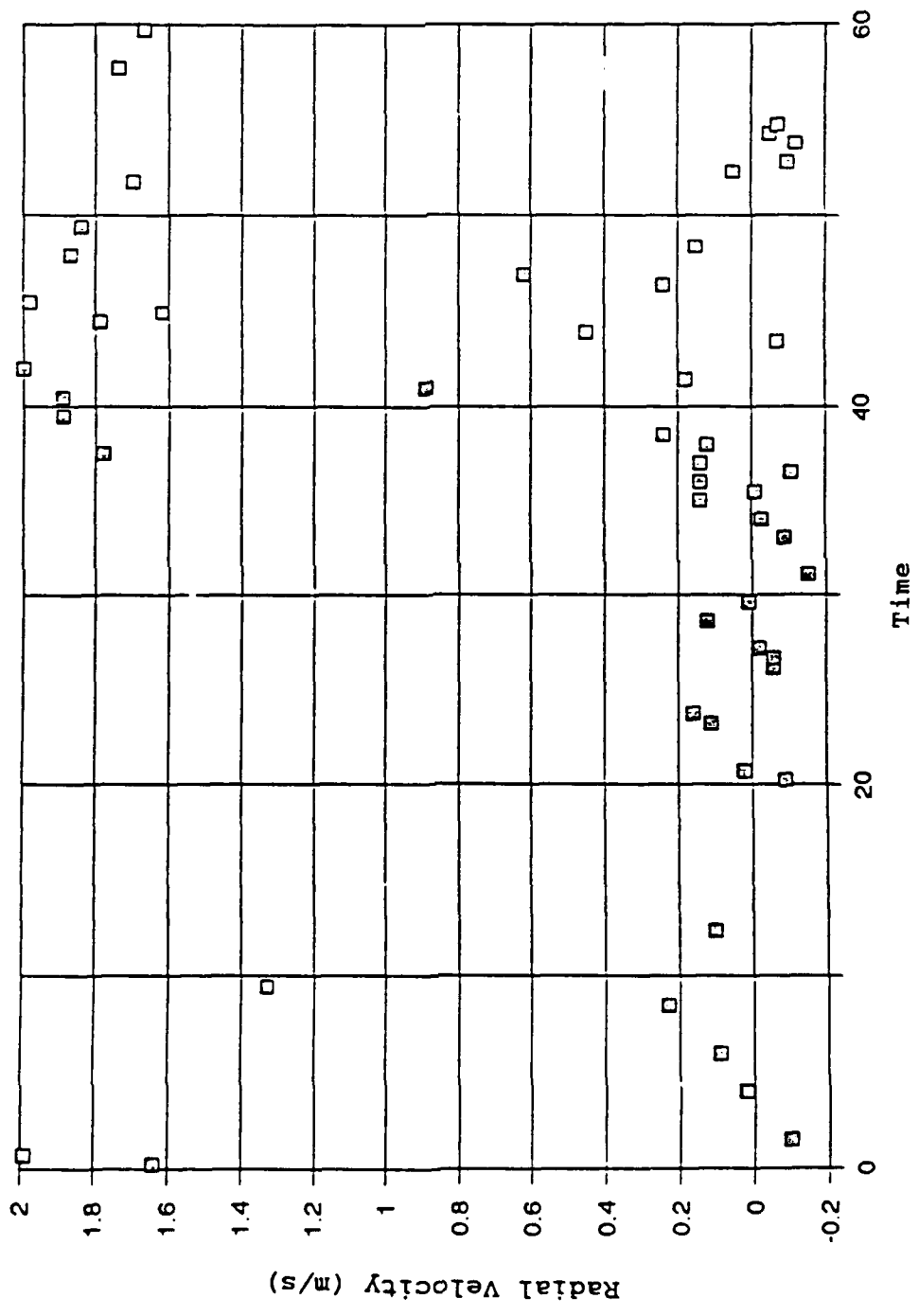profiler for 1700-1759 Z, 31 Jan 92, 0.71 km

Figure 4.6    Time series of radial velocities from the 915 MHz
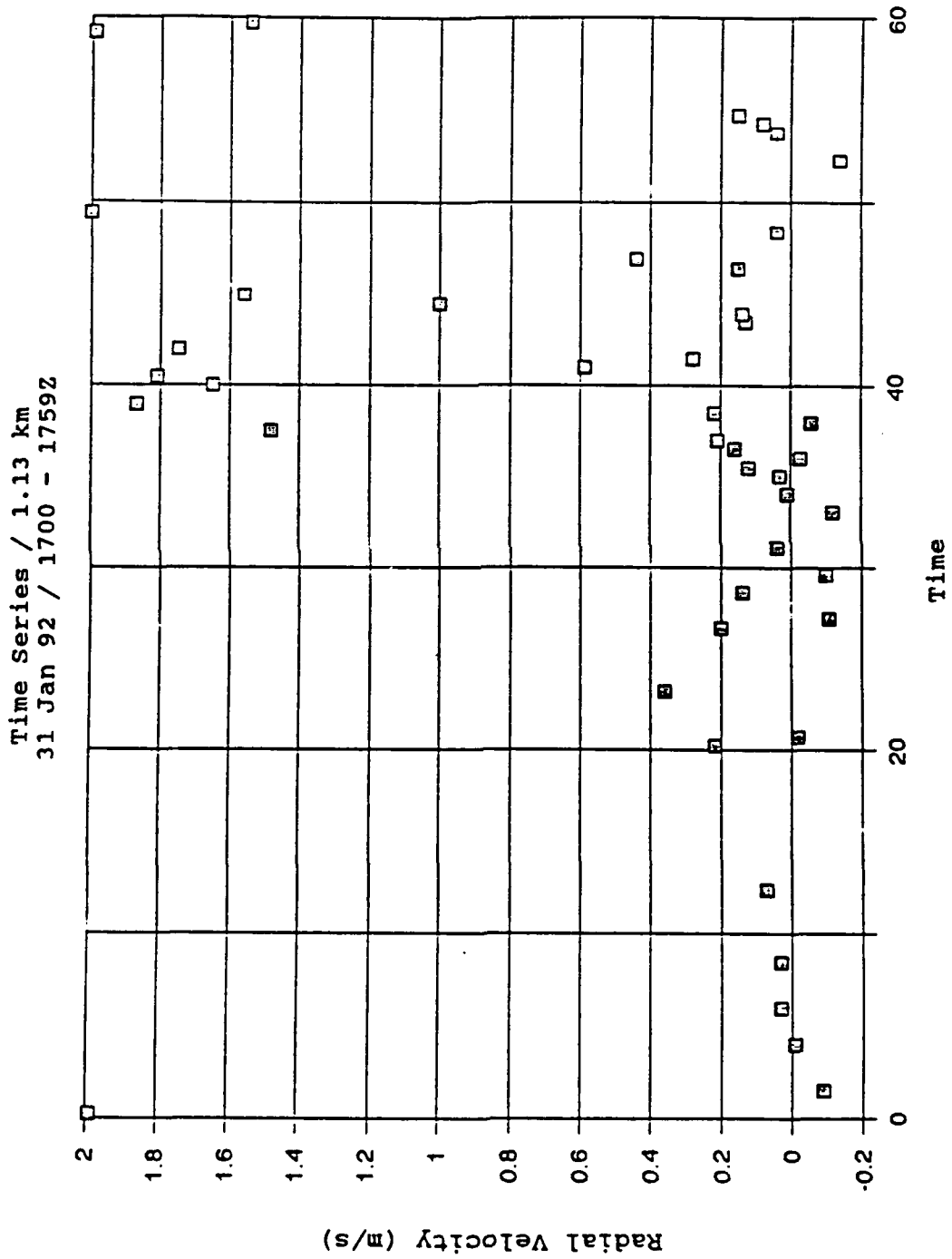profiler for 1700-1759 Z, 31 Jan 92, 0.92 km

44



Figure 4.7  Time series of radial velocities from the 915 MHz profiler for 1700–1759 Z, 31 Jan 92,  1.13 km
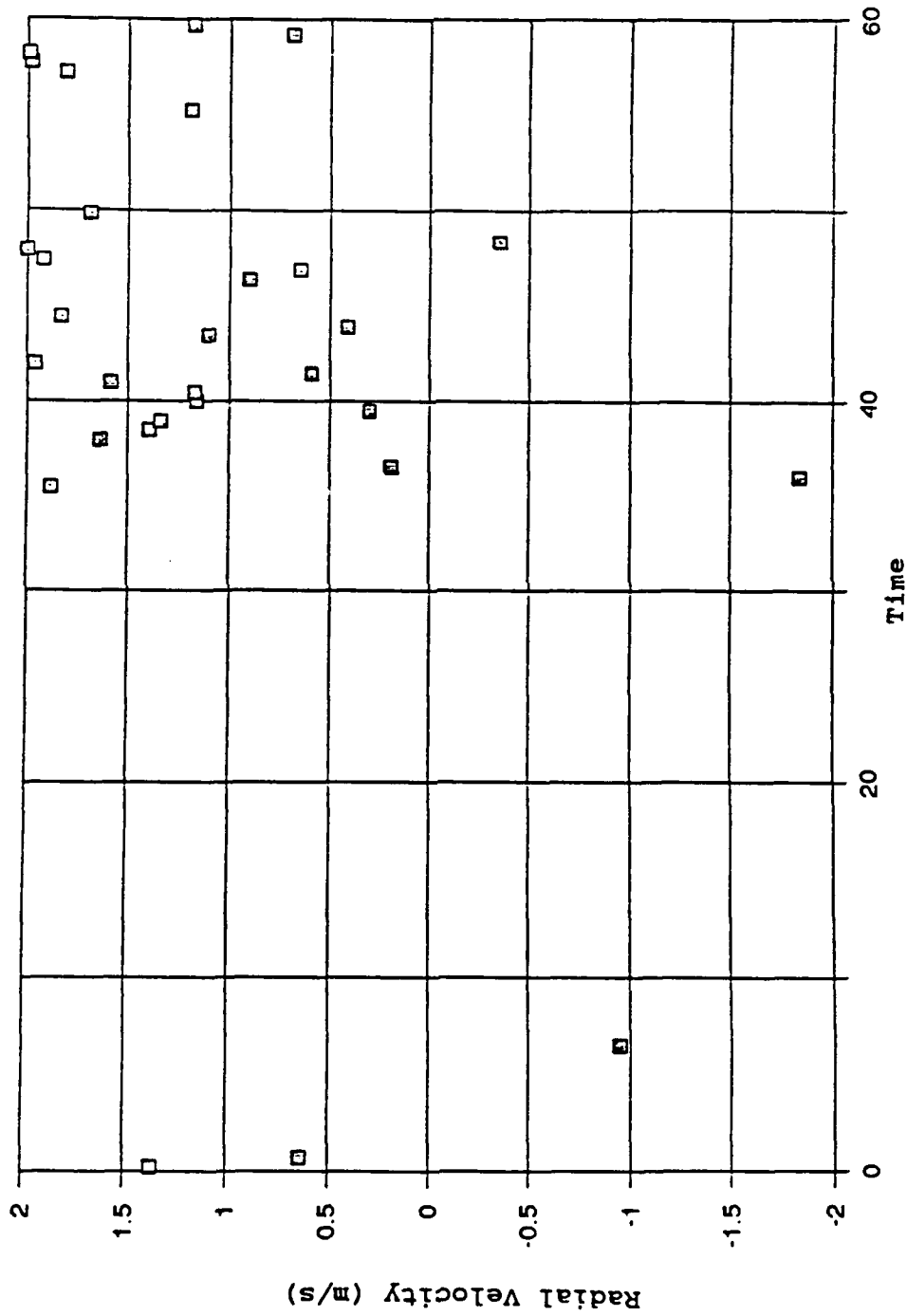
Figure 4.8  Time series of radial velocities from the 915 MHz profiler for 1700-1759 Z, 31 Jan 92, 1.34 km
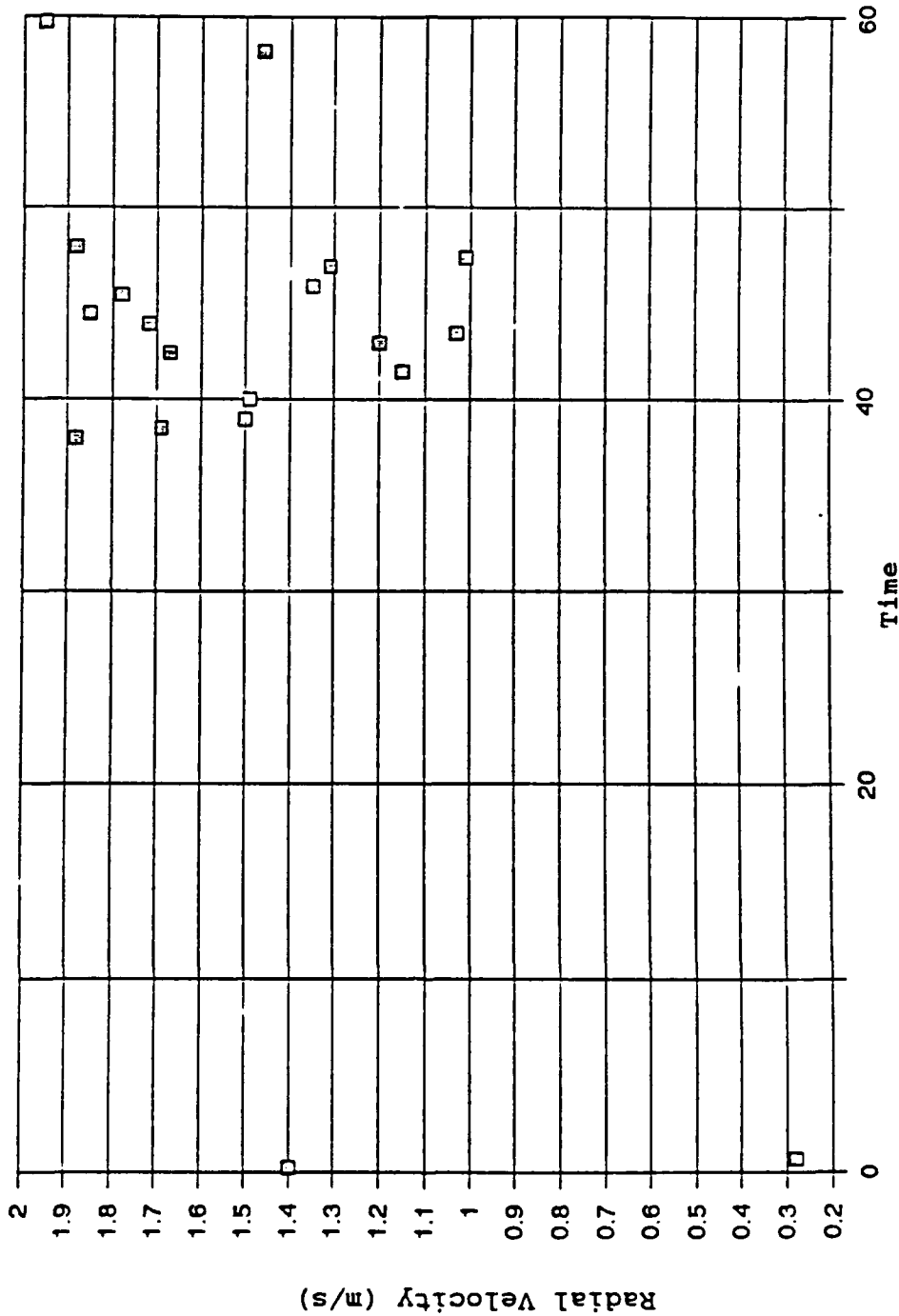
Figure 4.9  Time series of radial velocities from the 915 MHz
profiler for 1700-1759 Z, 31 Jan 92, 1.55 km

freezing level and from the vertical velocities around 2 m/s that the precipitation was frozen. Graupel particles, for example, have typical fall speeds of 1 to 2.5 m/s (Rogers & Yau, 1989).

Precipitation fall velocities continue to influence the profiler vertical velocities. As the height into the cloud increases (figures 4.6 to 4.8), the vertical velocity variance increases and is skewed towards positive radial velocity (downward motion). When well into the cloud base (figure 4.9), the precipitation fall velocities totally dominate the series.

Precipitation fall velocities are preferentially measured because the reflectivity from frozen precipitation particles is greater than that of "clear-air". A second peak in the spectra representing the "clear-air" vertical velocities may well be overlooked by the "peak-picking" algorithm in favor of the peak representing the more highly reflective frozen precipitation.

Visual inspection of the time series indicate a natural break at 1 m/s between clear air vertical velocities and precipitation fall velocity. Figure 4.10 shows a comparison of 915 MHz data before and after the 1 m/s precipitation filter. At all heights, the average 1 m/s filtered data have values less than the original 2 m/s filtered data. Far below the cloud base, the lowest two gates (0.51 Km and 0.61 Km) agree closely as a result of the tight grouping of vertical

**915 comparisons**
**31 jan 92/1700z**



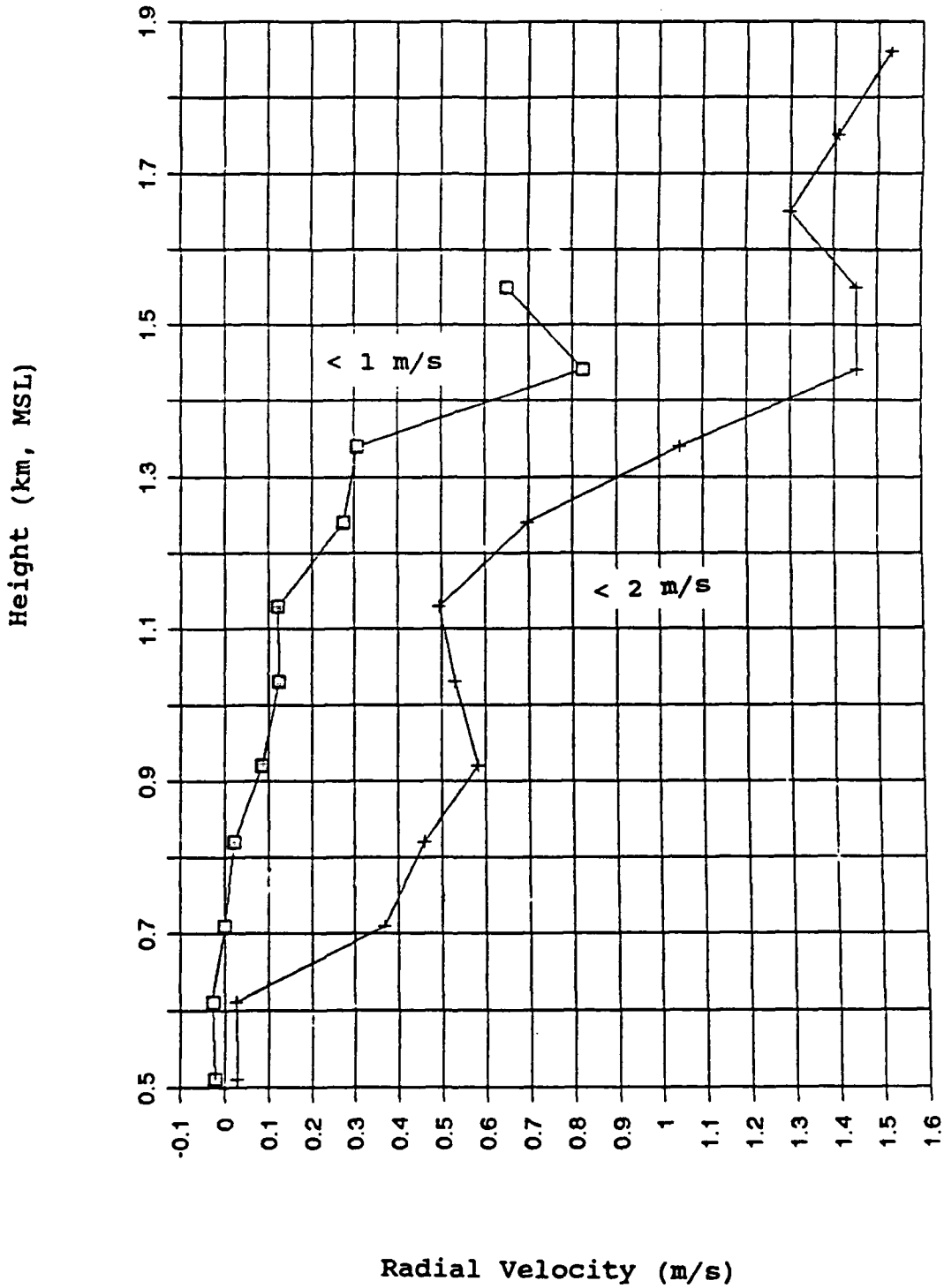Height (km, MSL)

< 1 m/s

< 2 m/s

Radial Velocity (m/s)

Figure 4.10 Comparison of 915 MHz profiler vertical velocities before and after 1 m/s precipitation filter

velocities. Above these bottom gates and into the cloud base, as the variability increases, the difference between filtered 915 MHz data and unfiltered 915 MHz data also increases. Precipitation-induced downward vertical velocities thus totally dominate the statistics above the lowest two gates. As a result, precipitation fall velocity was removed from the statistical analysis. However, if too much precipitation is present, the "clear-air" variance may not be estimated very well.

The advantage to this precipitation filter is that the hourly averaged vertical velocities of a non-precipitating cloud-topped boundary layer can be analyzed. The primary disadvantage is that the number of usable data are decreased. Initially, non-filtered data should yield 120 points at 30 second intervals for each hour. Table 4.3 summarizes the number of remaining data after each filtering step.

Signal loss with height is the most prevalent cause for data loss. Note that the signal is completely lost above 1.86 Km. As a result of this filtering, the 915 MHz profiler was unable to reach the top of the cloud. Additional filtering of precipitation fall velocities reduce this maximum height to only 1.44 Km. Dashed lines (--) indicate that no filtered data were available at that height. Note that only 4 observations remained at 1.44 Km after the filtering process. Confidence in the statistics for this gate was, thus, substantially reduced.

Table 4.3:  Summary of remaining usable data after filtering
for the 915 MHz wind profiler, 31 January 1992, 1700 Z.

| Gate | Height | Unfiltered | SNR Filter | Precipitation Filter |
|------|--------|------------|------------|---------------------|
| 1 | 0.51 | 120 | 39 | 36 |
| 2 | 0.61 | 120 | 37 | 36 |
| 3 | 0.71 | 120 | 45 | 36 |
| 4 | 0.82 | 120 | 47 | 36 |
| 5 | 0.92 | 120 | 51 | 36 |
| 6 | 1.03 | 120 | 45 | 34 |
| 7 | 1.13 | 120 | 44 | 34 |
| 8 | 1.24 | 120 | 34 | 23 |
| 9 | 1.34 | 120 | 30 | 10 |
| 10 | 1.44 | 120 | 23 | 4 |
| 11 | 1.55 | 120 | 19 | -- |
| 12 | 1.65 | 120 | 16 | 2 |
| 13 | 1.75 | 120 | 4 | -- |
| 14 | 1.86 | 120 | 5 | -- |
| 15 | 1.96 | 120 | -- | -- |

Figure 4.11 shows a comparison of 915 MHz and 404 MHz data, after precipitation filtering, for the same hour period. At the lowest levels, where 915 MHz and 404 MHz data can be compared (between 0.78 km and 0.92 km), the 915 MHz profiler vertical winds are in agreement with the 404 MHz profiler winds.  Above this level, the 915 MHz profiler still produces higher magnitude vertical velocities than the 404 MHz profiler.

## 4.2.3  Horizontal Wind Contamination

Initial analysis of 20 Mar 91 data indicate a possible bias in the vertical beam of the 915 MHz vertical wind profiles.  Comparisons of 915 MHz and 404 MHz vertical
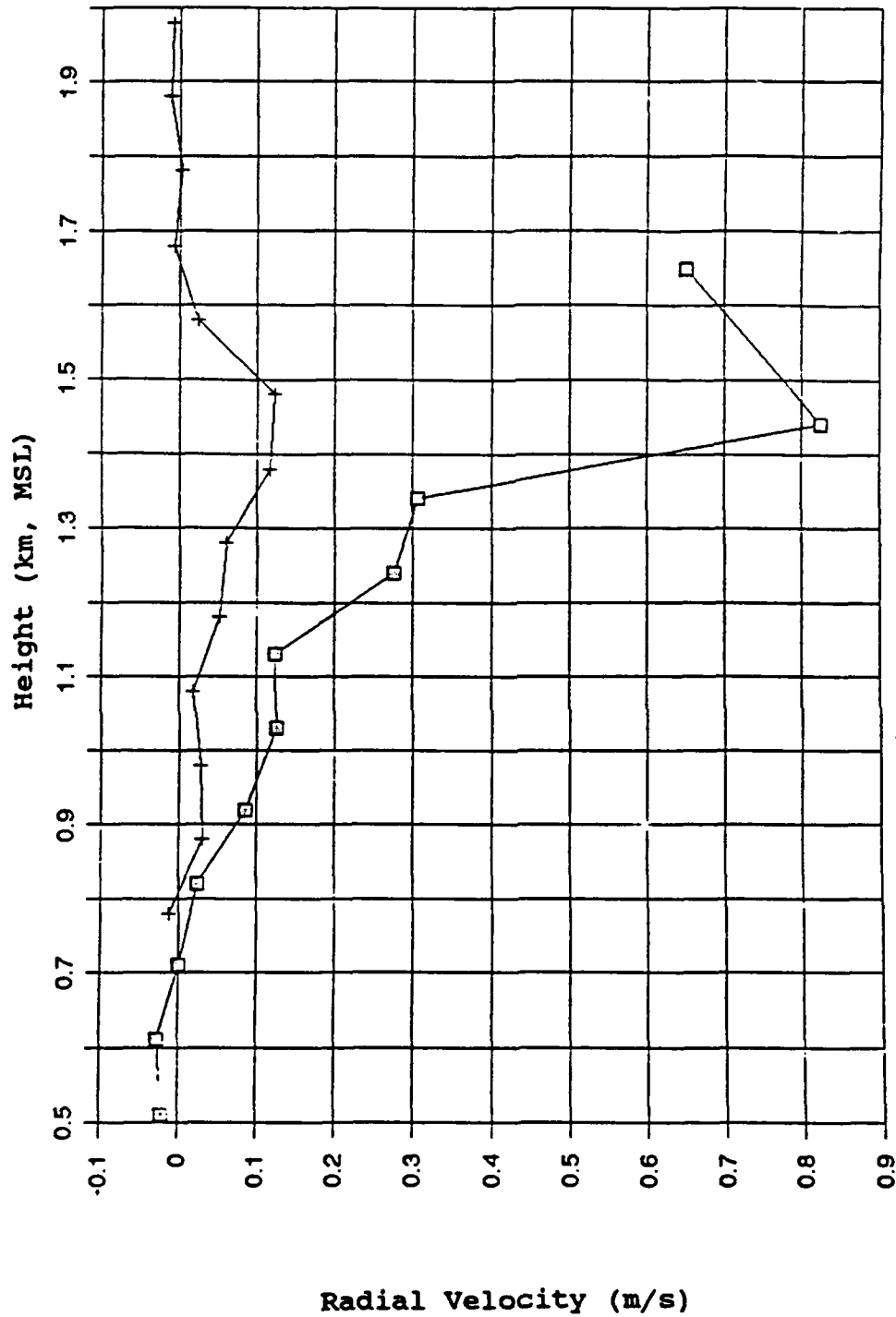
Figure 4.11   Comparison of 915 MHz and 404 MHz data, after
              precipitation filtering for 31 Jan 92, 1700Z

velocity profiles averaged over the same time periods indicate a persistent increase in 915 MHz average velocities.

Figures 4.12 and 4.13 are profiles of hourly averages of horizontal wind speed and direction for 31 January 1992, for the hours of 14 Z, 15 Z, and 16 Z.  Each gate represents 7-13 data averaged for a one hour period.  At 1400 Z, wind speed remains a nearly constant 5 m/s from 0.78 km to 1.44 km (figure 4.12).  Speed decreases at 1.44 km from ~4.5 m/s to a minimum of 3 m/s at 1.75 km.  Wind direction backs with height from 318° at 0.87 km to 300° at 1.54 km, with a great deal of directional variability, possibly the result of light wind speeds (figure 4.13) or persistent thermal winds in that layer.  A corresponding jump in 915 MHz vertical velocities is noted (figure 4.14) from 1.13 km to a peak at 1.34 km.  Note; however, figure 4.14 does not represent data filtered to omit vertical velocities greater than 1 m/s (precipitation filter). With only 2-3 observations per gate above 1.13 km, the validity of determining horizontal wind contamination above this height is questionable.  When one omits vertical velocity values greater than 1 m/s (figure 4.15), increased vertical velocity values still persist above 0.71 km.  Note from figure 4.12 that wind speed increases to a nearly constant 5 m/s value in the layer between 0.77 and 0.87 km.

The above evidence clearly indicates that the 31 January 1991, 915 MHz vertical velocity data are contaminated with horizontal winds.  It is possibly the result of an "angular"
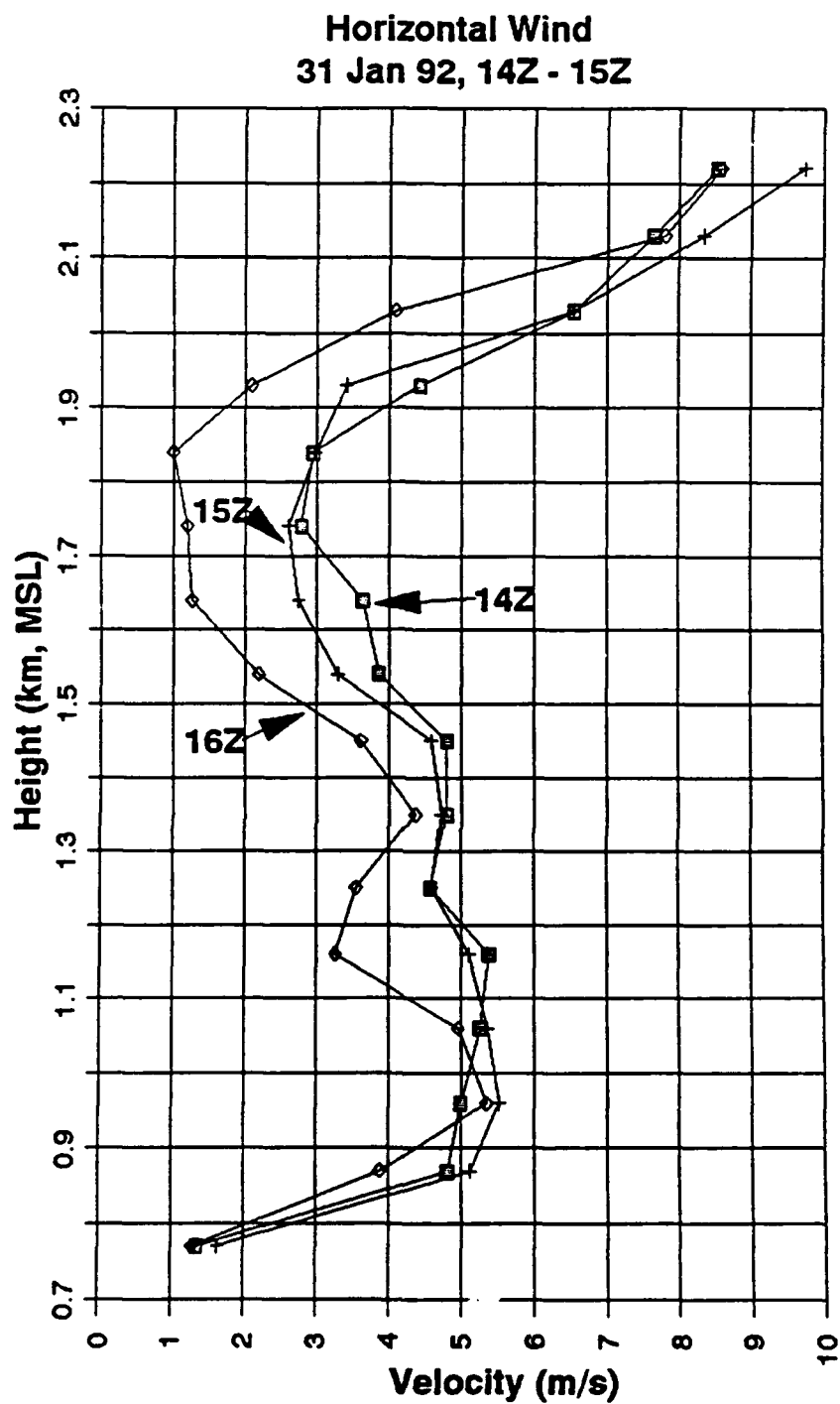
Figure 4.12    Horizontal wind speed from the 404 MHz wind
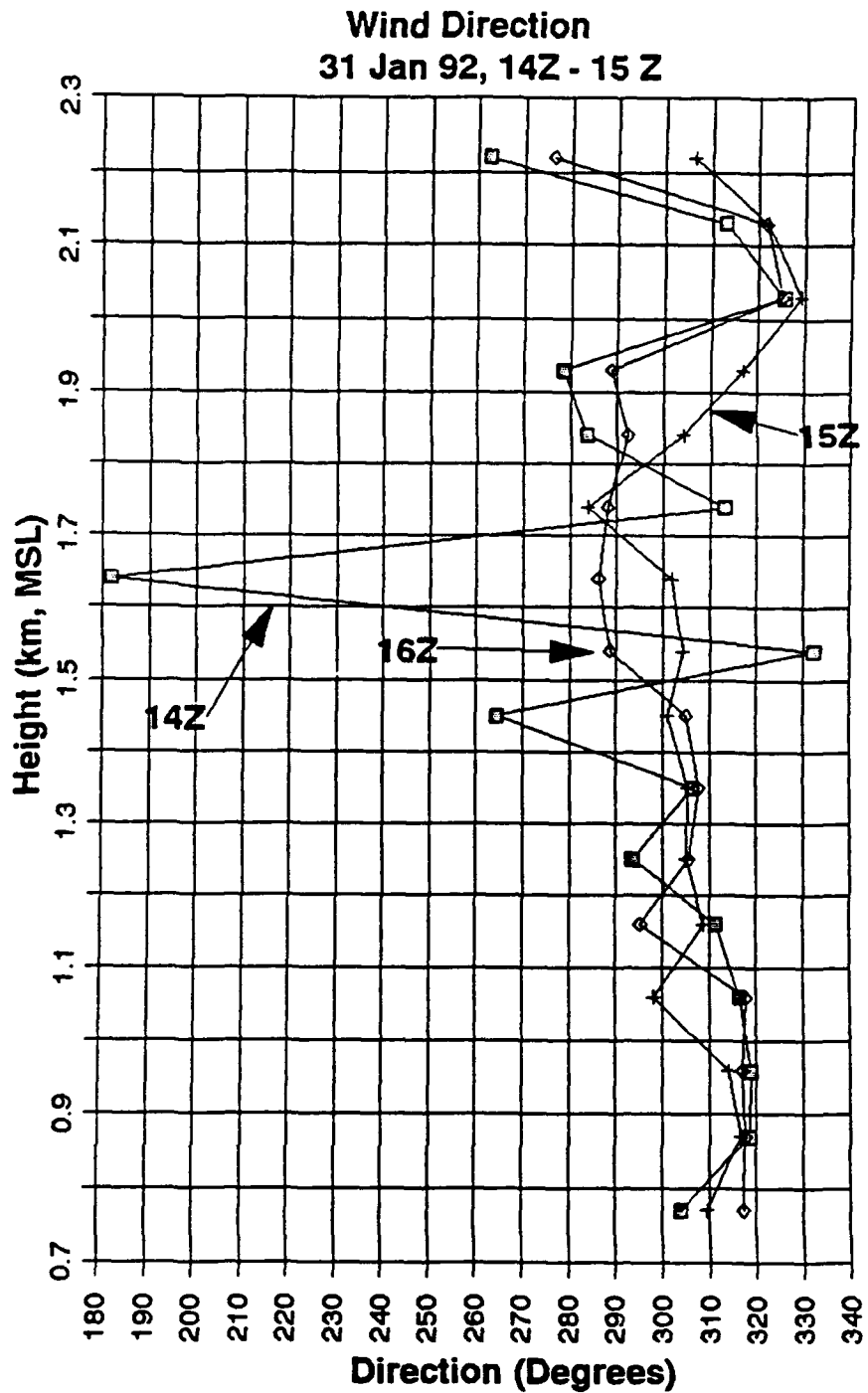               profiler for 31 Jan 92, 14 Z, 15 Z, and, 16 Z

Figure 4.13  Wind direction from the 404 MHz wind profiler for
31 Jan 92, 14 Z, 15 Z, and 16 Z

915 MHz/404 MHz Radial Velocity
31 Jan 92, 1400 Z
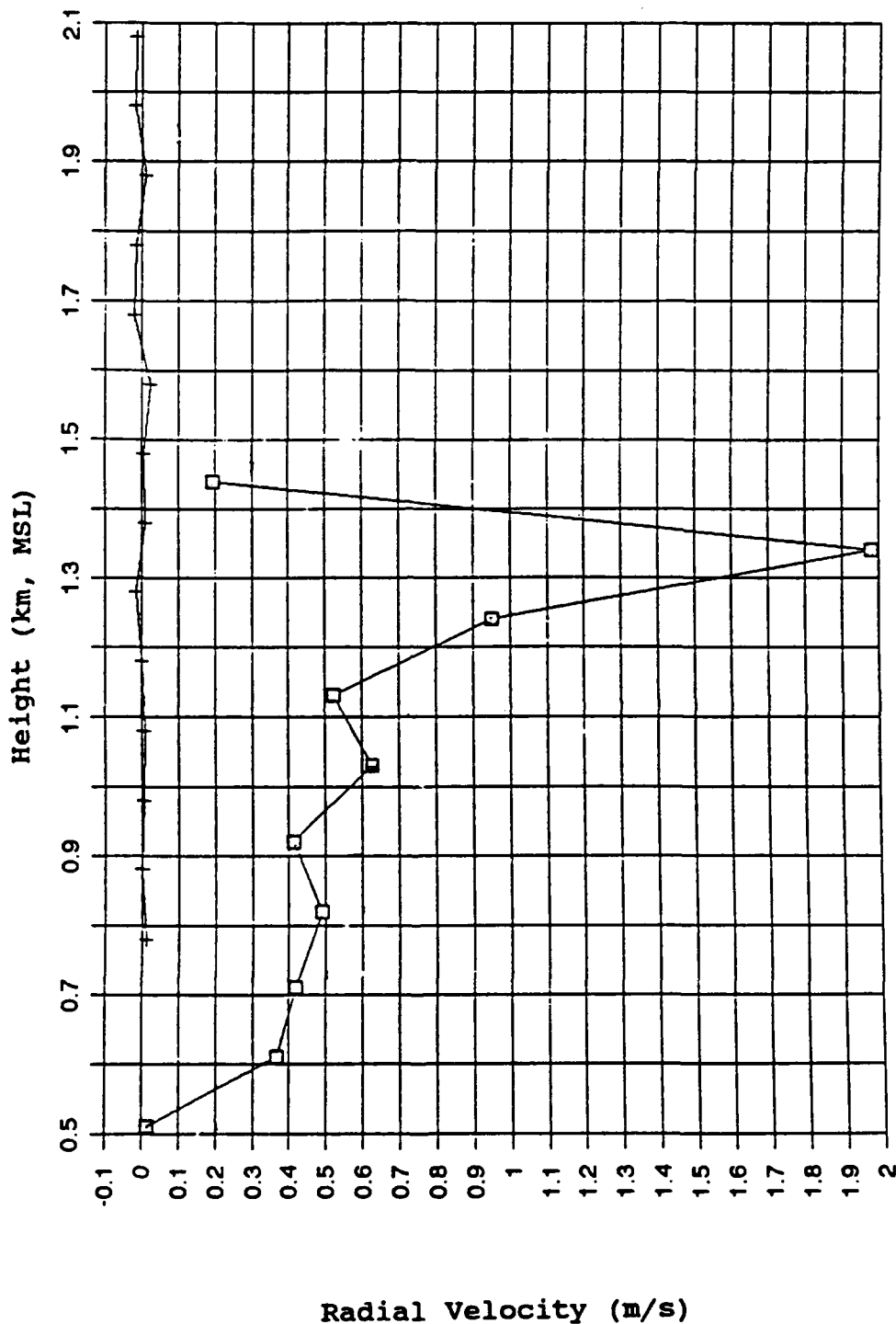


Radial Velocity (m/s)

Figure 4.14 Comparison of 915 MHz and 404 MHz radial velocities prior to precipitation filtering for 31 Jan 92, 14 Z
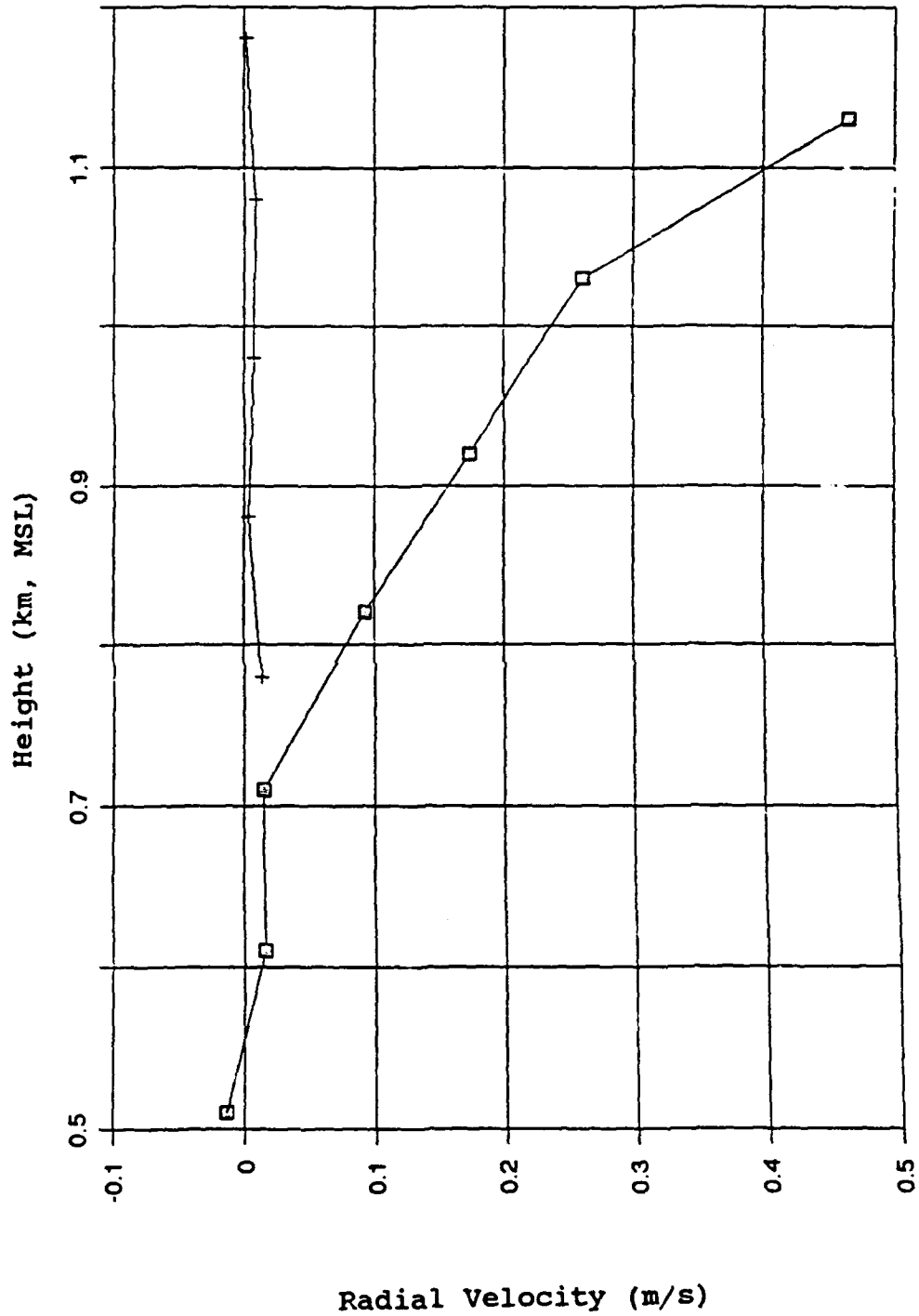
Figure 4.15   Comparison of 915 MHz and 404 MHz radial
              velocities after precipitation filtering for
              31 Jan 92, 14 Z

bias in the vertical beam of the profiler. There is, unfortunately, insufficient information to determine the exact cause of the bias. Unfortunately, the 915 MHz profiler had been disassembled and reassembled between the observation periods. The likelihood of similar bias angle errors between data sets is remote. Most probably, a subtle tilt in the zenith beam antenna, possibly due to installation limitations (or, perhaps, frost heave) is probably the cause of zenith angle errors. Determination of this angle error requires a statistical correlation analysis of horizontal winds (direction and magnitude) vs. vertical velocity bias over several synoptic time periods to eliminate random error.

## 4.3 Results

Data from the 20 March 91, 915 MHz profiler were determined to be false representations of the true vertical velocities. Evaluation of 20 Mar 91, 1900 Z - 2000 Z vertical velocities, measured by the 915 MHz and 404 MHz profilers, revealed a substantial gap in the 915 MHz vertical velocities (figure 4.16). In figure 4.16, circles represent the 404 MHz profiler vertical velocities, and the crosses represent the 915 MHz profiler vertical velocities. Velocities between ± 0.6 m/s are suspiciously absent from the 915 MHz time series. Further investigation revealed that a previously undetected "zero suppression" filter had been activated on the 915 MHz
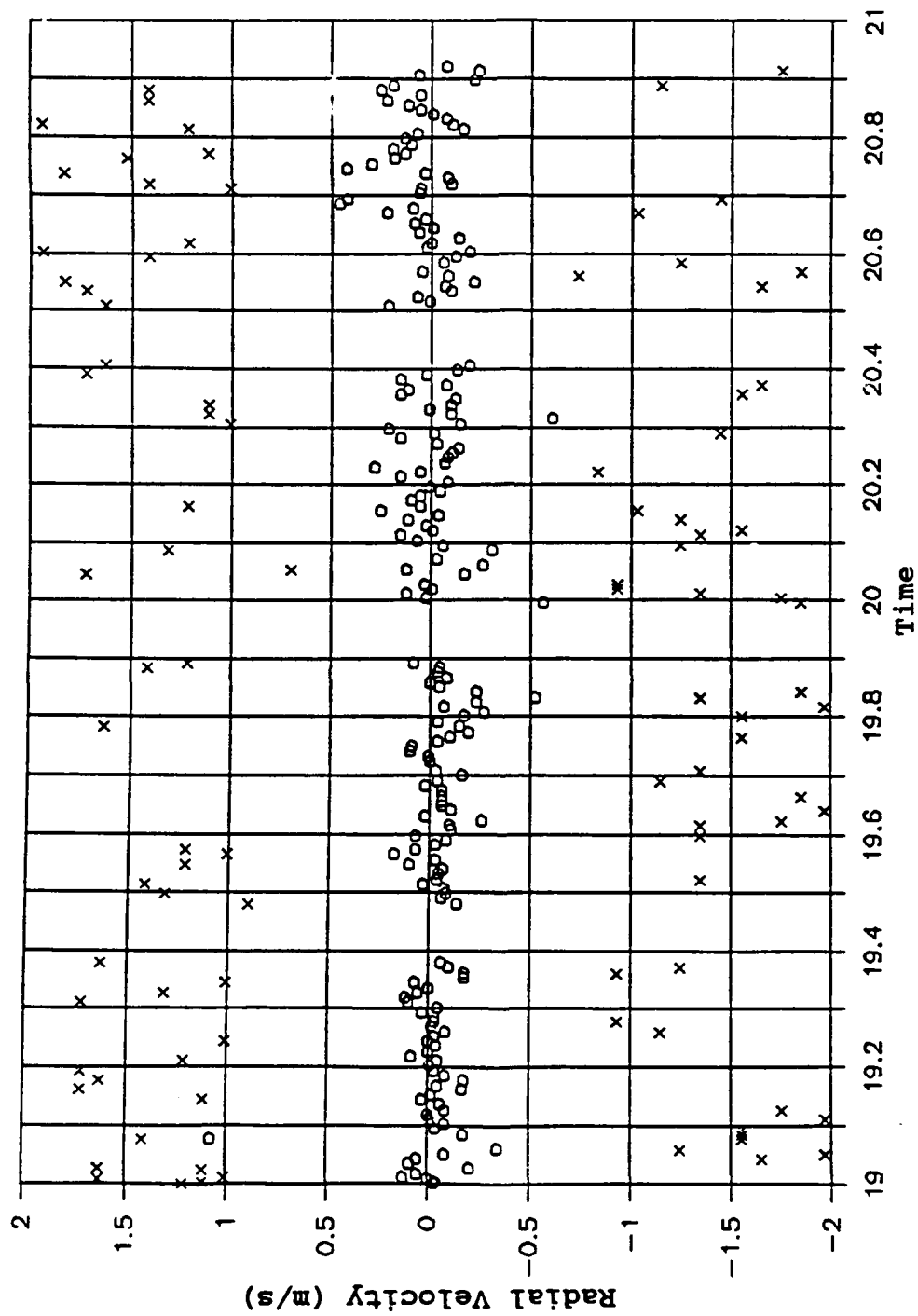
Figure 4.16  Time series of 915 MHz vertical velocities revealing zero suppression filtering for 20 Mar 91, 1900 - 2000Z.  Circles represent 404 MHz radial velocities, crosses represent ≤15 MHz radial velocities

profiler. The zero suppression filter effectively suppressed vertical velocities ± 2 FFT bins about the zero vertical velocity bin. With a 9.99 m/s maximum radial velocity based on the Nyquist frequency, and a 64 point FFT, a 0.3122 m/s per FFT bin was eliminated from the data along the 5 FFT bins. This resulted in an approximately ± 0.63 m/s gap in the vertical velocities. The algorithm used to choose the spectral peak, as a result of the zero suppression filter, inevitably picked fictitious (biased) vertical velocity values larger than the true vertical velocities.

Williams and Thomson (1986) identified zero suppression biases in measurements of low wind velocities using Penn State's VHF wind profiler. Their study showed that zero suppression in the presence of wind velocities below 6 m/s systematically biased the horizontal wind results. An artificial increase in absolute wind velocities occur when the spectral peaks fall within the specified range of FFT points about the zero point. Biases as large as 2 m/s were measured in a range of ± 6 m/s. Average biases were from 0.79 to 1 m/s.

Once the 20 March 1991, 915 MHz data had been processed with zero suppression, post processing yielded no further clues into the true nature of the vertical velocities. The data is lost. As a result, all subsequent analysis will be from the high temporal resolution 404 MHz data of 20 Mar 91.

The radiosonde and ceilometer data of 20 Mar 91 indicate

a 14 Z cloud base at 1200 m MSL, and cloud top at 1450 m MSL. Ceilometer measurements also indicate a 74% cloud cover for the 14 Z hour. The number of high temporal 404 MHz measurements after SNR and aircraft ($\geq$ 2 m/s omitted) filtering vary around 90 observations per gate per hour. This is sufficient to statistically interpret the data with a reasonable degree of confidence.

Figure 4.17 is a profile of 404 MHz radial velocities. Positive velocity is downward motion towards the radar, and negative velocity is upward motion away from the radar. Two notable features are evident with this profile. First is the large peak in downward motion located at the 1.38 km gate. Within the resolution of the profiler, this corresponds well with the radiosonde estimated inversion base of 1450 m. Preferential sampling of relatively high reflectivity within inverted plumes may occur because the "peak-picking" algorithm chooses the highest power peak (associated with the downward motion of the inverted plume), rather than a second weaker peak associated with the more widely spread (and less reflective) compensating upward motion. This preferential, high reflectivity, sampling is exemplified by relatively large downward motion with no detection of compensating upward motion.

High reflectivity of the inverted plume may be caused by at least two phenomena. First, air from cloud top, containing frozen precipitation-sized particles, entrained into the

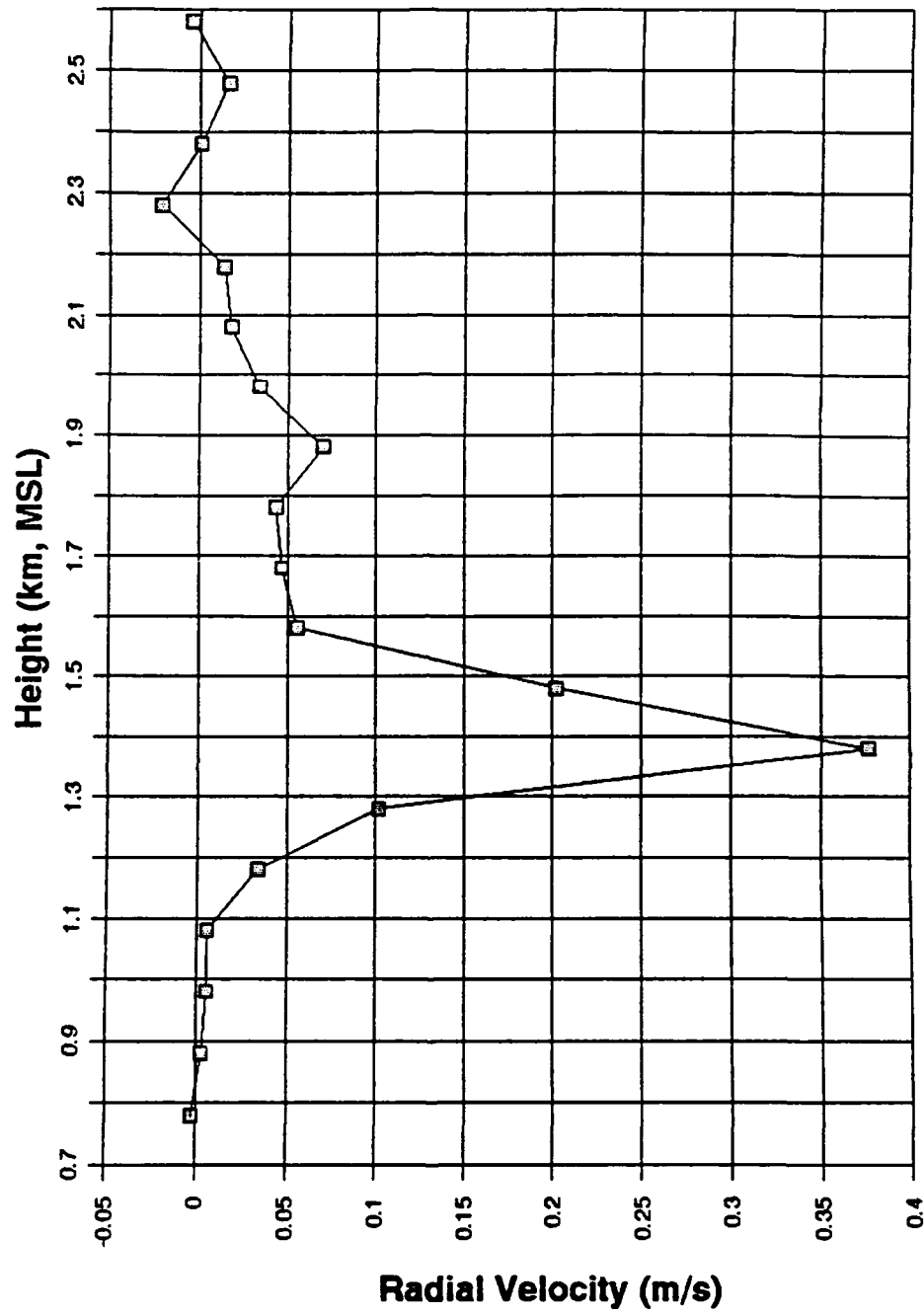**20 Mar 91, 1400z**
**Vertical Velocity**



Figure 4.17   Radial velocity from the 404 MHz profiler, 20 March 1991, 14 Z

downward plume could cause a relatively high reflectivity within the plume. However, if this were the case, one would expect to see the top of the cloud layer as being equally as reflective as the inverted plume. A second possibility for relatively high reflectivity within the inverted plume is the result of entrained free atmosphere air from above the cloud mixing with cloudy air. Recall from equation (17) that reflectivity is proportional to $C_n^2$. $C_n^2$ is a function of the temperature and moisture functions. In the relatively small area of the inverted plume, the turbulent mixing of entrained free atmosphere and boundary layer air produce a high $C_n^2$, which in turn produces a high reflectivity. These explanations must remain conjectural until simultaneous spectra and profiler measurements of cloud-topped boundary layers become available.

Breaking waves at cloud top may assist the free atmosphere to entrain into the boundary layer. Richter (1969) identified, using MST-CW radar, a wave like phenomenon at cloud top with evidence of breaking waves. The wave amplitudes were as small as 10 m to 14 m and their spatial wavelengths were unknown. Breaking waves will form at cloud top when there is shear and dynamic instability.

Large wind shear across the top of the 20 March 1991 mixed layer at 16 Z and 20 Z indicate that the conditions for Kelvin-Helmholtz waves may have existed at 14 Z. No radiosonde winds were available for 14 Z; however, figures

14.18 and 14.19 indicate that at 16 Z, a shear zone from 1.2 km to 1.8 km and a directional shear from 1.2 km to 1.6 km exists. A Richardson number near a critical value of about 0.25 (Stull, 1988) is necessary for unstable conditions to prevail. Using 14 Z temperatures and 16 Z radiosonde winds, a Richardson number estimate is 0.26. However, this estimation of Richardson number at 14 Z is inadequate, among other things. because the balloon measured winds were at 16 Z.

The second notable feature in figure 4.17 is the large zone of subsidence from 0.8 km to 2.2 km. Such large scale subsidence is the result of convergence aloft, and divergent motion below. The 20 Mar 91, 12 Z 850mb and 700mb NMC synoptic analysis indicate a ridge aloft extending from the Great Lakes to Florida in a NW-SE orientation with a convergent pattern over Pennsylvania. The NMC Surface analysis for 12 Z indicates a divergent pattern over the Pennsylvania area. Thus, the observation of large scale subsidence is at least synoptically plausible.

Figure 4.20 is the 404 MHz profile of vertical velocity variance. Notably, a peak in vertical velocity variance occurs at the 1.38 km gate coincident with the inversion base and the peak in vertical velocity. In the presence of cloud-top evaporative cooling, one expects to find such a peak in vertical velocity variance.

Another plausible explanation for this variance peak at cloud top is from the increased mean and possible sampling
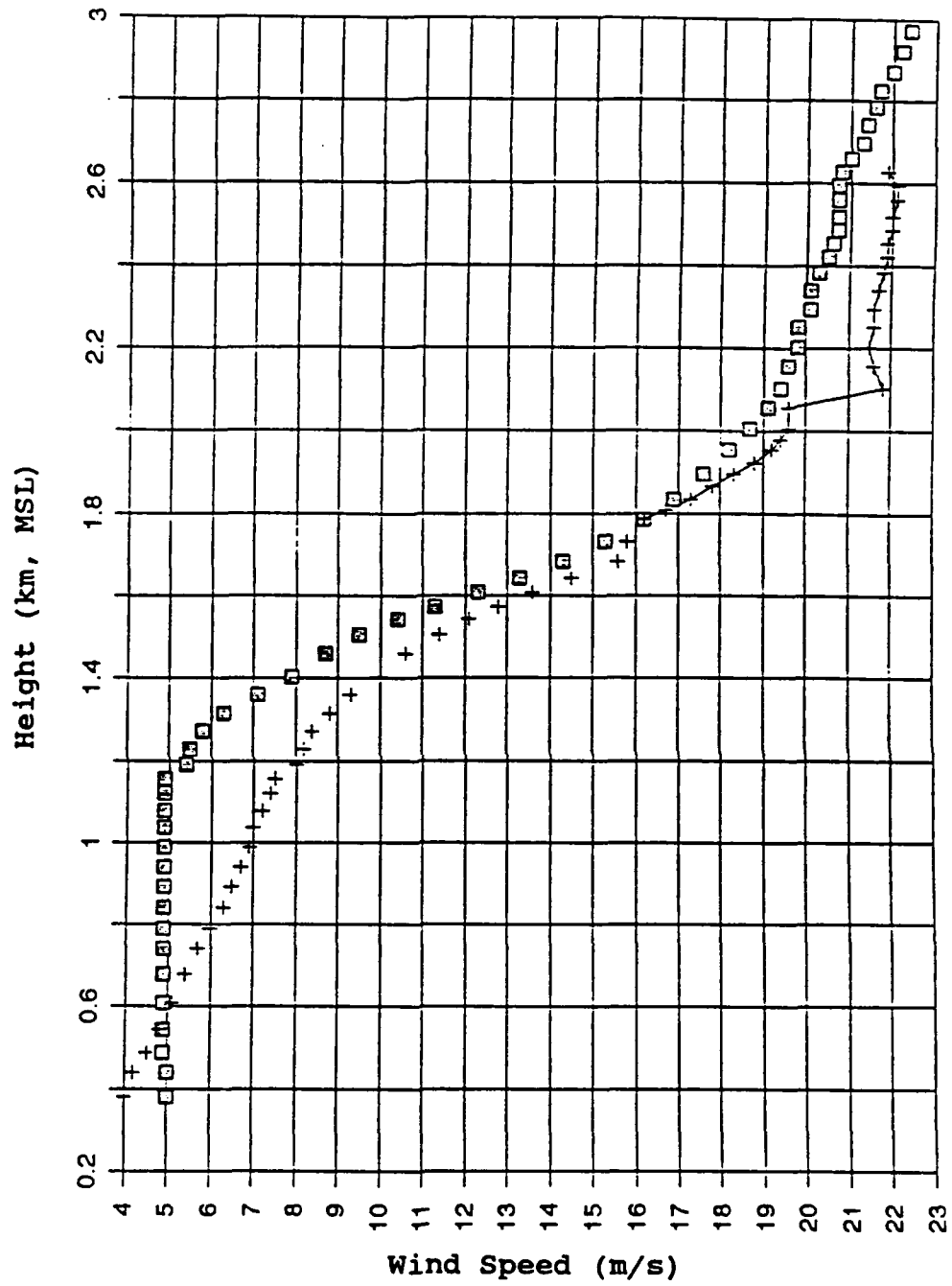
Figure 4.18   Radiosonde wind speed for 20 Mar 91, 1643 Z and
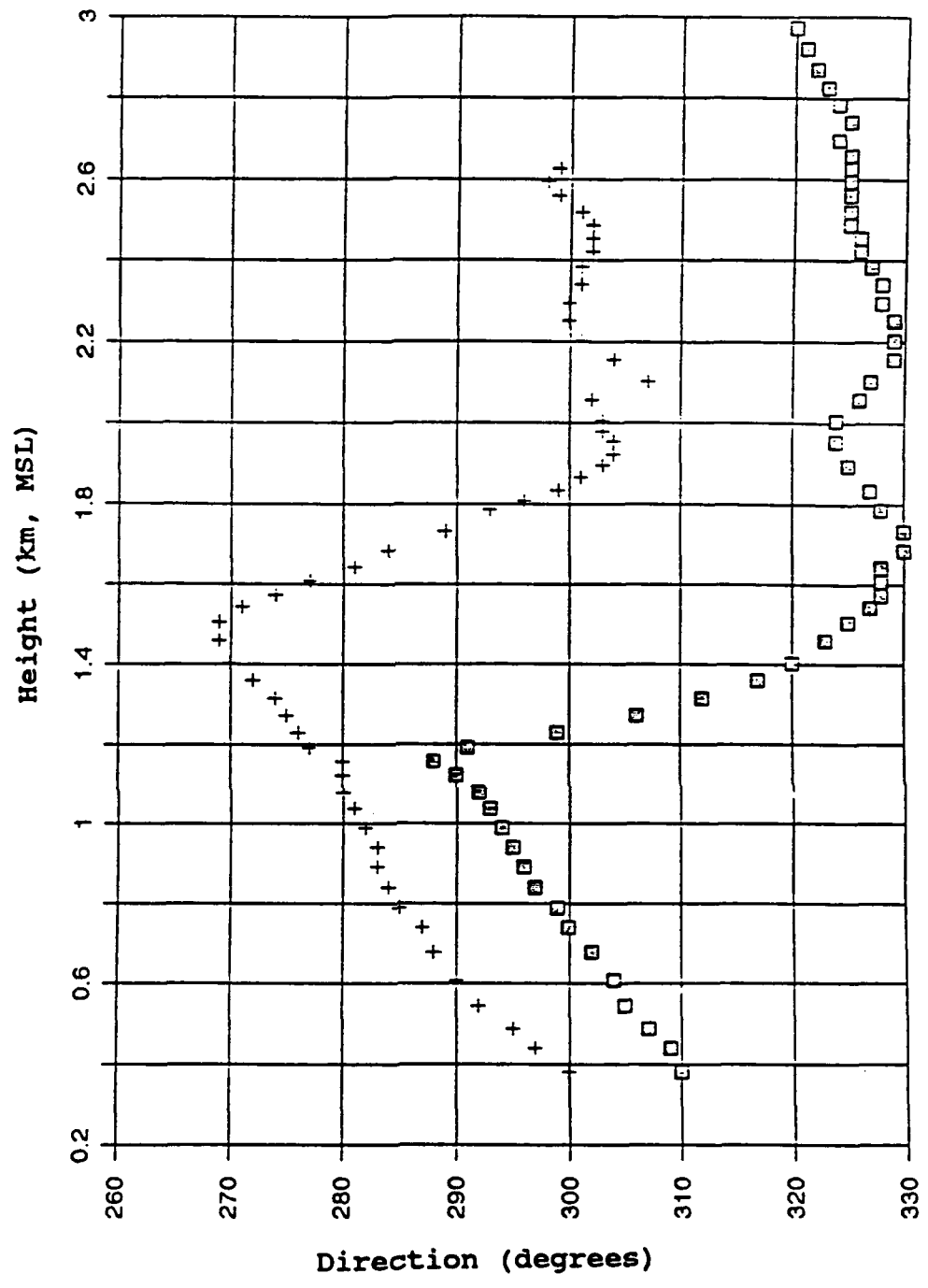2000 Z.   Squares: 1634 Z, Crosses: 2000 Z

Figure 4.19   Radiosonde wind direction for 20 Mar 91, 1634 Z
             and 2000 Z.   Squares: 1634 Z, Crosses: 2000 Z

**20 March 1991 (14Z)**
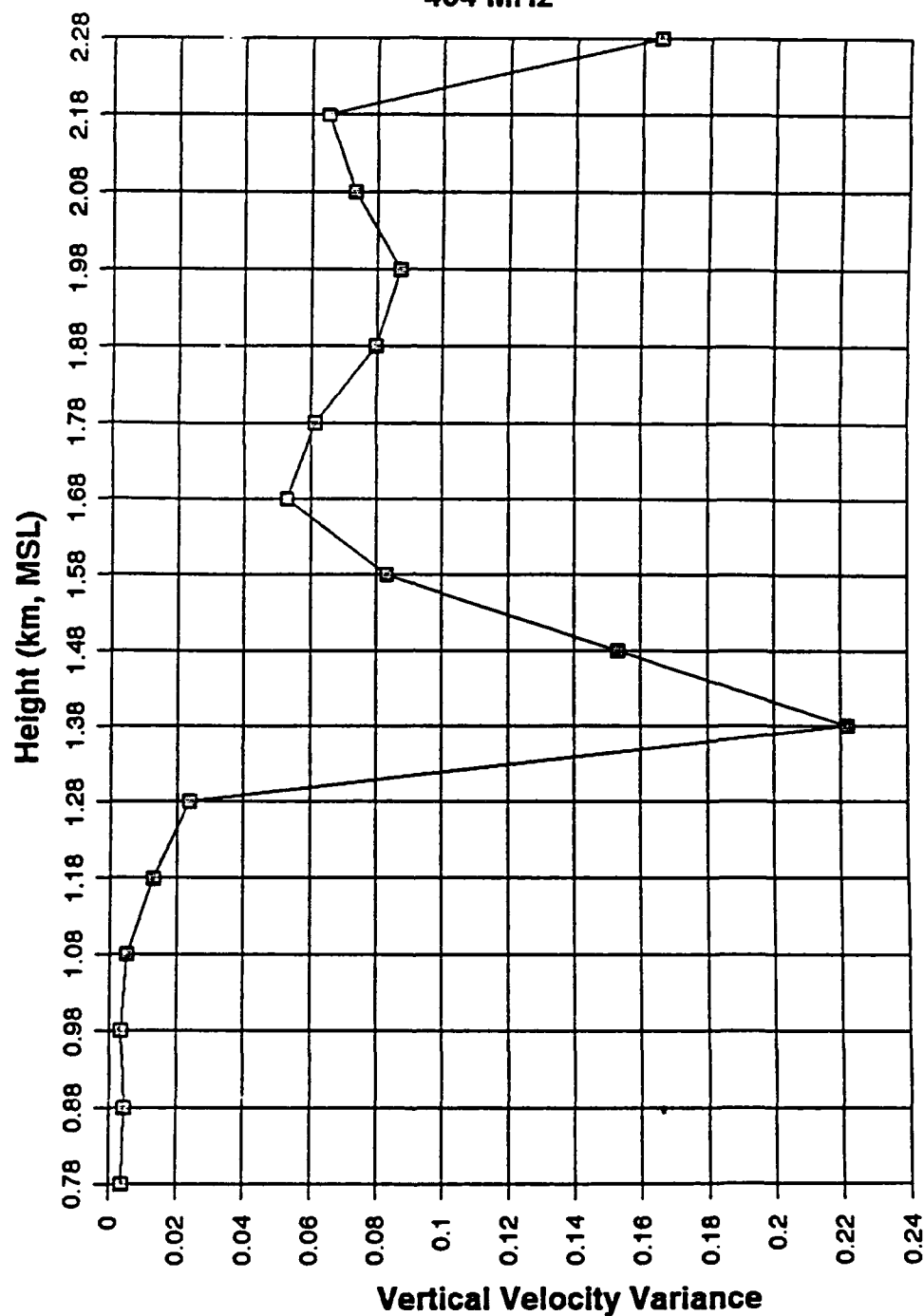**404 MHz**



Figure 4.20   Variance in 404 MHz vertical velocities for
              20 Mar 91, 14 Z

errors as a result of undulating cloud top height. Figures 4.21, 4.22, and 4.23 are selected time series of 14 Z vertical velocities at 1.08 km, 1.38 km, and 1.58 km. The mean vertical velocity centers at nearly 0 m/s at the 1.08 km height, in a tight grouping at about ± 0.1 m/s. At 1.38 km, near mean cloud top, the mean vertical velocity has a much greater magnitude at a downward vertical velocity of ~0.35 m/s with a widely dispersed grouping. Above this level at 1.58 km, the mean settles back to ~ 0 m/s with the excursions about the mean returning to about ±0.1 m/s. The sampling volume at a constant height of 1.38 km may enter and exit the undulating cloud top and continue to preferentially measure large downward vertical velocities as a result of the previously hypothesized highly reflective inverted plumes. This type of preferential sampling would also lead to an increased vertical velocity variance by combined low vertical velocity free atmosphere and relatively high vertical velocity boundary layer measurements from the inverted plume within the hour. Further evidence of this phenomenon exists in the 404 MHz, 14 Z, Signal-to-Noise (SNR) profiles.

Figure 4.24 is a profile of the hourly averaged, range corrected SNR for the 14 Z hour. At cloud top (1450 m), there is a notable minimum in SNR. One would expect the clear air SNR to be less than the cloud filled volume. This implies that the SNR minimum at 1.48 km may be the result of preferential clear air measurements above the cloud top.
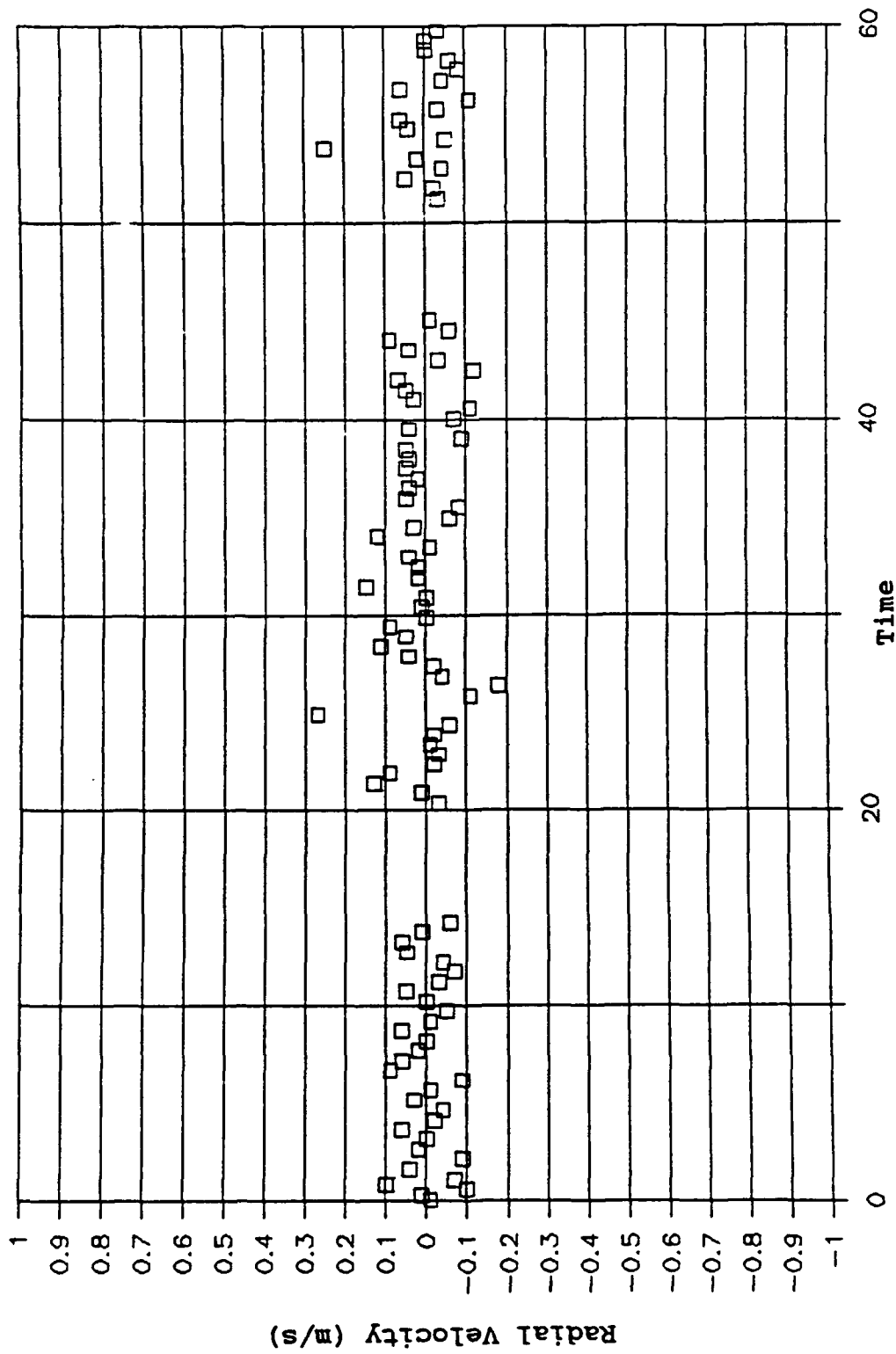
Figure 4.21   Time series of 404 MHz radial velocities for
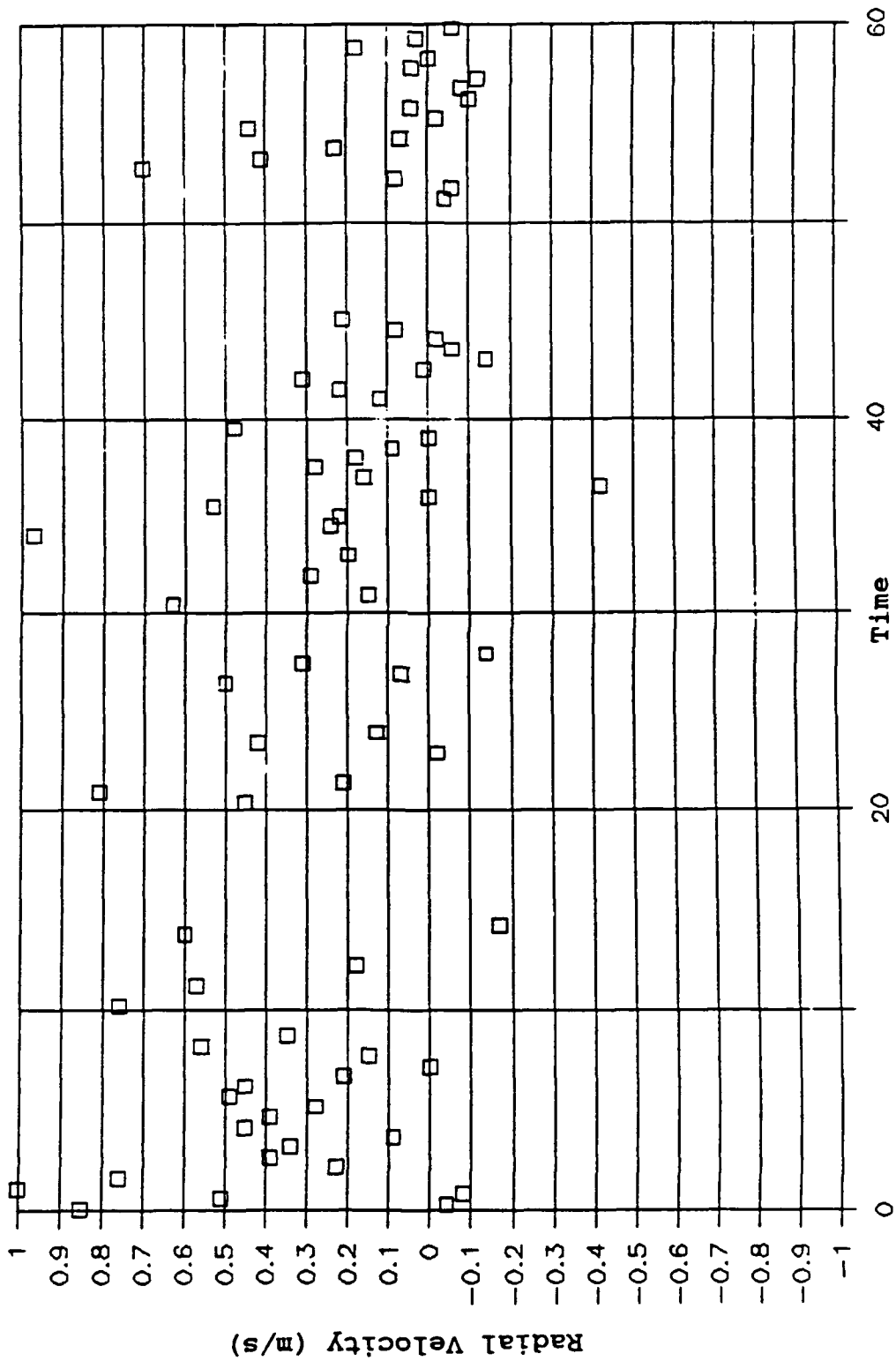20 Mar 91, 14 Z, 1.08 km

68

Figure 4.22   Time series of 404 MHz radial velocities for
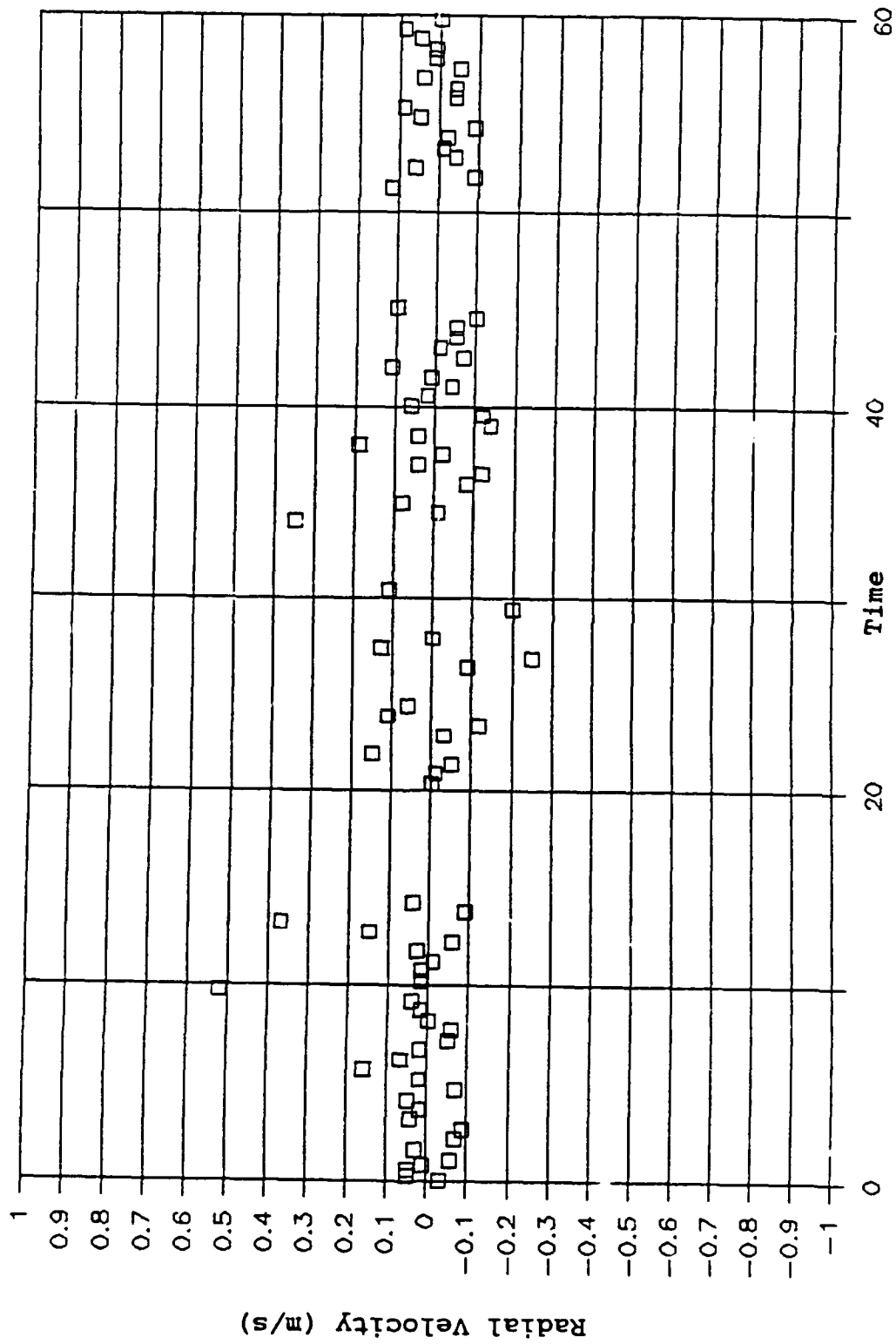20 Mar 91, 14 Z, 1.38 km

Figure 4.23   Time series of 404 MHz radial velocities for
20 Mar 91, 14 Z, 1.58 km
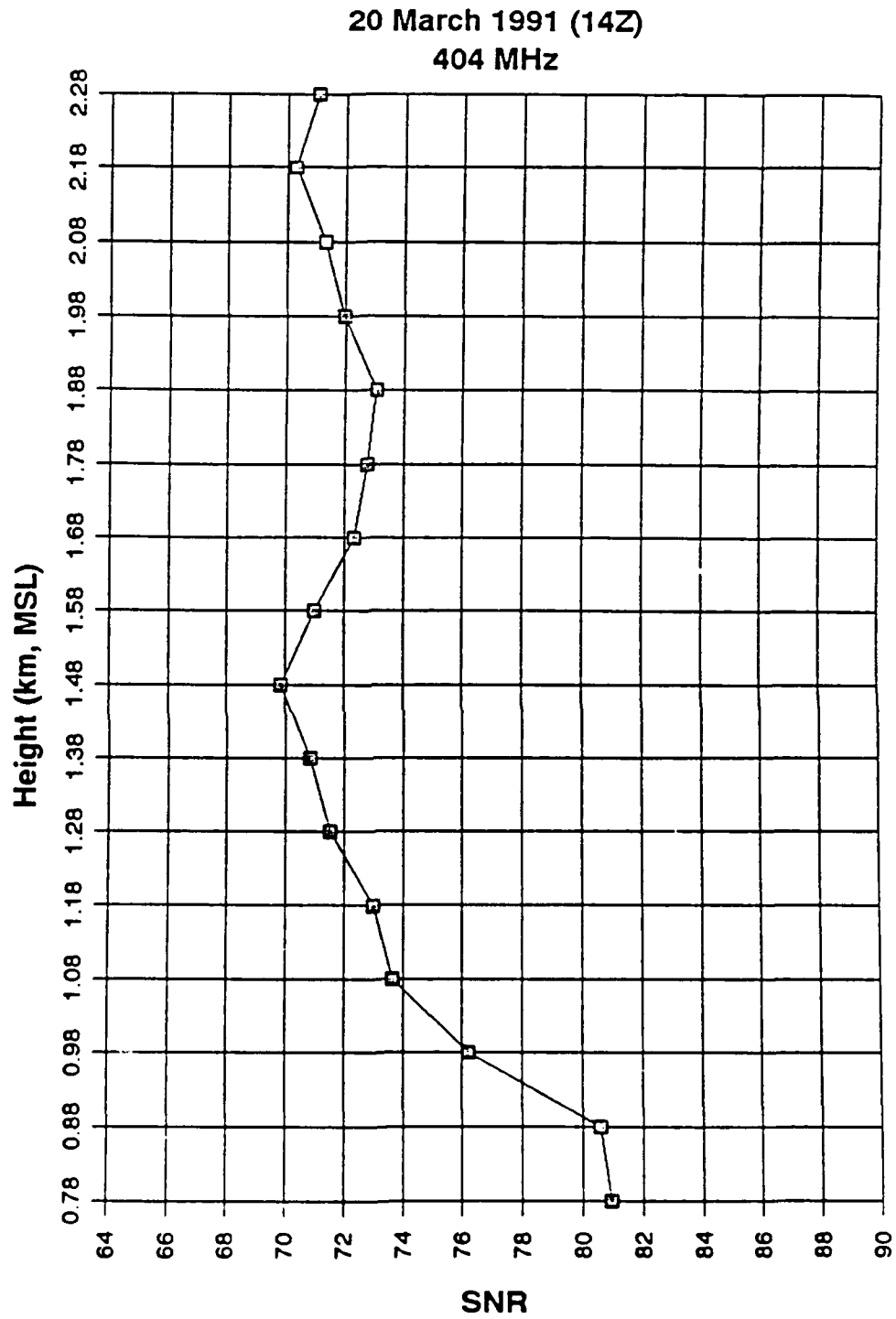
**20 March 1991 (14Z)**
**404 MHz**

Figure 4.24   Range corrected SNR for 20 Mar 91, 14 Z

Additionally, figure 4.25 is the vertical profile of the variance in SNR for the same period. A minimum in SNR variance occurs between the 1.48 km and 1.58 km gates and a maximum at the 1.38 km gate.

Intermittent sampling of clear air, above cloud top along with cloudy air, would tend to reduce the mean SNR, and increase the SNR variance. For Rayleigh scatters, radar reflectivity is proportional to the number of scatterers in the radar volume. As the number of scatterers decrease, reflectivity also decreases. Thus, one would expect the mean clear air SNR to be less than the mean cloudy air SNR. A mix of clear and cloudy air will produce a mean SNR at a value between the cloudy SNR and the clear SNR. However, the SNR variance will be larger for the mixed air than the clear or cloudy air as a result of the increased range of values between the clear air measurements and the cloudy measurements.

The 15 Z average profiles represent cloud coverage of approximately 50% during the hour. Cloud base height, as determined by the LCL, is 1.3 km. No radiosondes were launched during the 15 Z hour; however, interpolation between 14 Z and 16 Z cloud top heights imply average cloud top height is ~1500 m. The 15 Z, 404 MHz radial velocity (figure 4.26) shows an overall slight subsidence below 1.48 km. Mean radial velocities are decreased. A subtle peak in downward vertical velocity occurs at 1.28 km and another at 1.58 km coincident
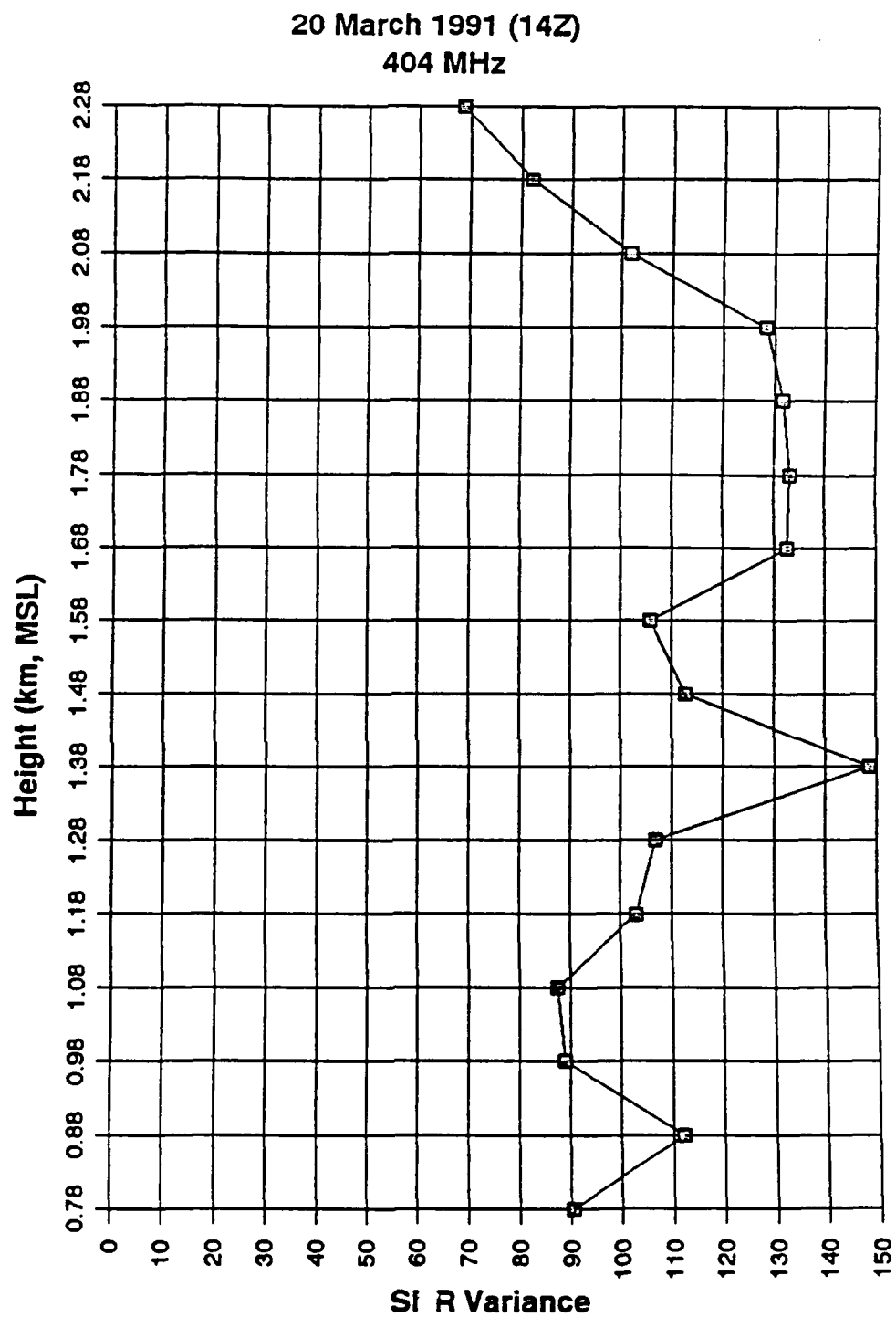
**20 March 1991 (14Z)**
**404 MHz**



Figure 4.25   Variance of SNR for 20 Mar 91, 14 Z
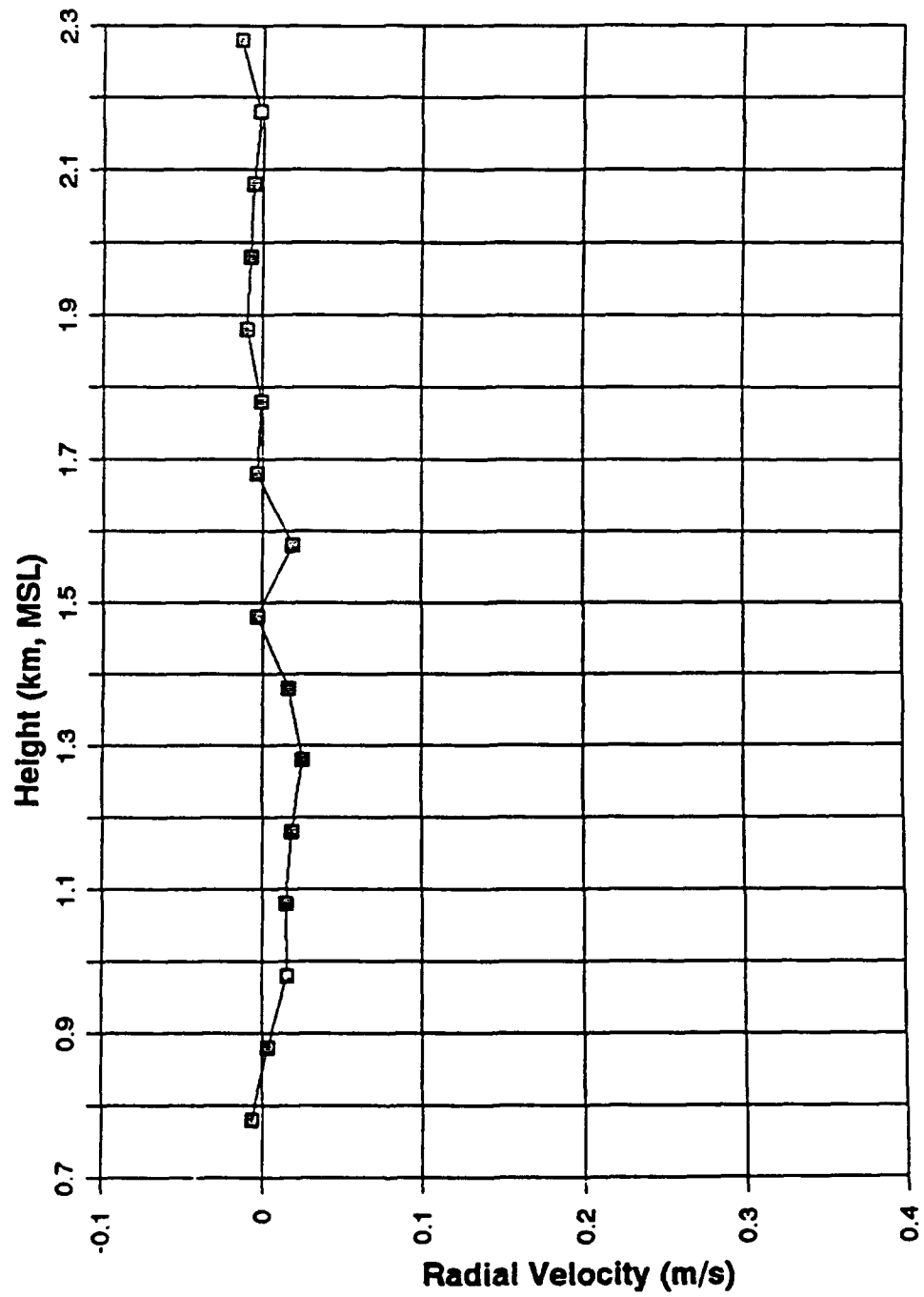
**20 March 1991 (15Z)**
**404 MHz**



Figure 4.26   Radial velocity from the 404 MHz profiler,
20 Mar 91, 15 Z

75

with cloud top. The vertical velocity variance (figure 4.27) shows a maximum at 1.48 km, coincident with cloud top height.

With only 50% cloud cover, increased solar heating may have caused the net downward vertical velocity to decrease from 1400 Z to 1500 Z. As the surface layer heated, rising plumes of relatively hot surface air mixed with the mixed layer air above to produce a larger $C_n^2$ than the surrounding subsiding air. This process is much like the high reflectivity inverted plumes from cloud top. The reflectivity in these rising plumes is higher than the surrounding subsidence area so the "peak-picking" algorithm chose the updraft peak. Thus, when averaged over an hour, the upward vertical velocity plumes dominate the statistics and decrease the mean downward velocities. Underwood (1981) presents sodar measurements which elucidate this phenomenon.

The 15 Z SNR profile (figure 4.28) is similar to the 14 Z profile with a minimum at 1.38 km and a maximum at 1.78 km. Figure 4.29 shows a peak in SNR variance at 1.48 km. Again, reminiscent of the 14 Z SNR profiles, a minimum in SNR near cloud top is evident, and is indicative of the sampling problem at cloud top. The mean SNR is reduced while its variance is increased as the clear air signal dominates in the sampled volume.

The 16 Z vertical velocity (figure 4.30) and vertical velocity variance (figure 4.31) profiles begin to indicate the presence of increased surface heating as a result of decreased

**20 March 1991 (15Z)**
**404 MHz**
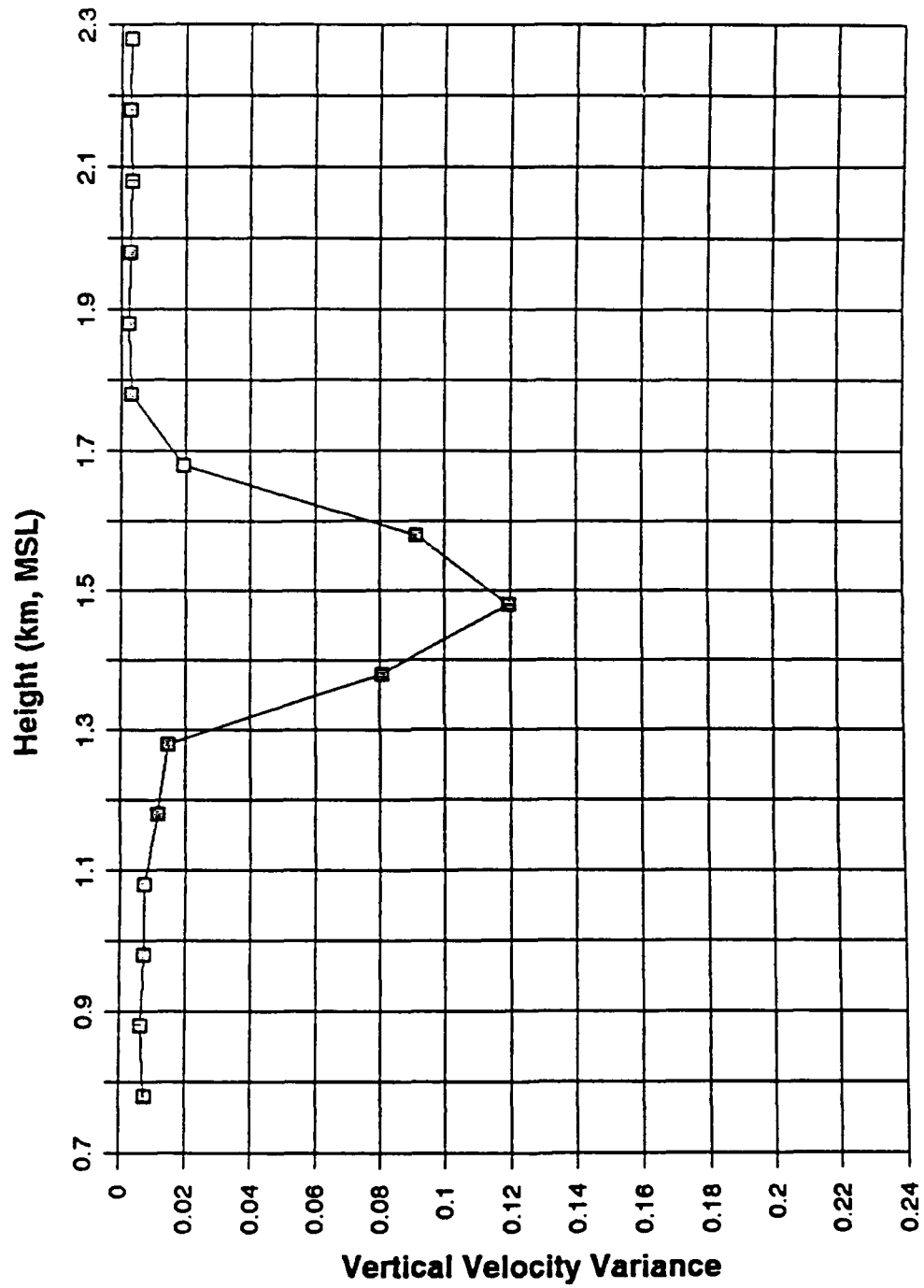


Figure 4.27   Variance in 404 MHz vertical velocities,
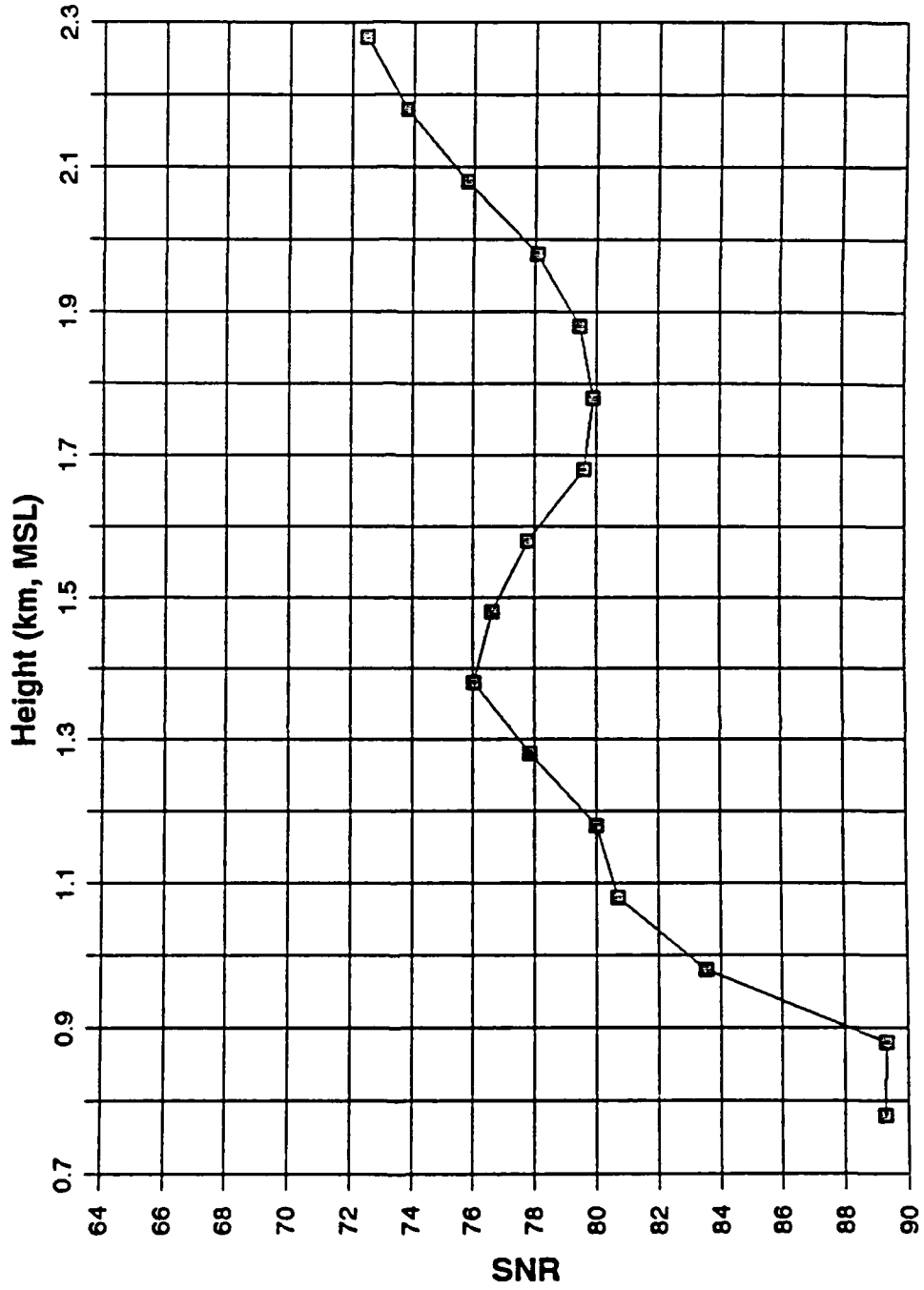20 Mar 91, 15 Z

**20 March 1991 (15Z)**
**404 MHz**



Figure 4.28   Range corrected SNR for 20 Mar 91, 15 Z

**20 March 1991 (15Z)**
**404 MHz**



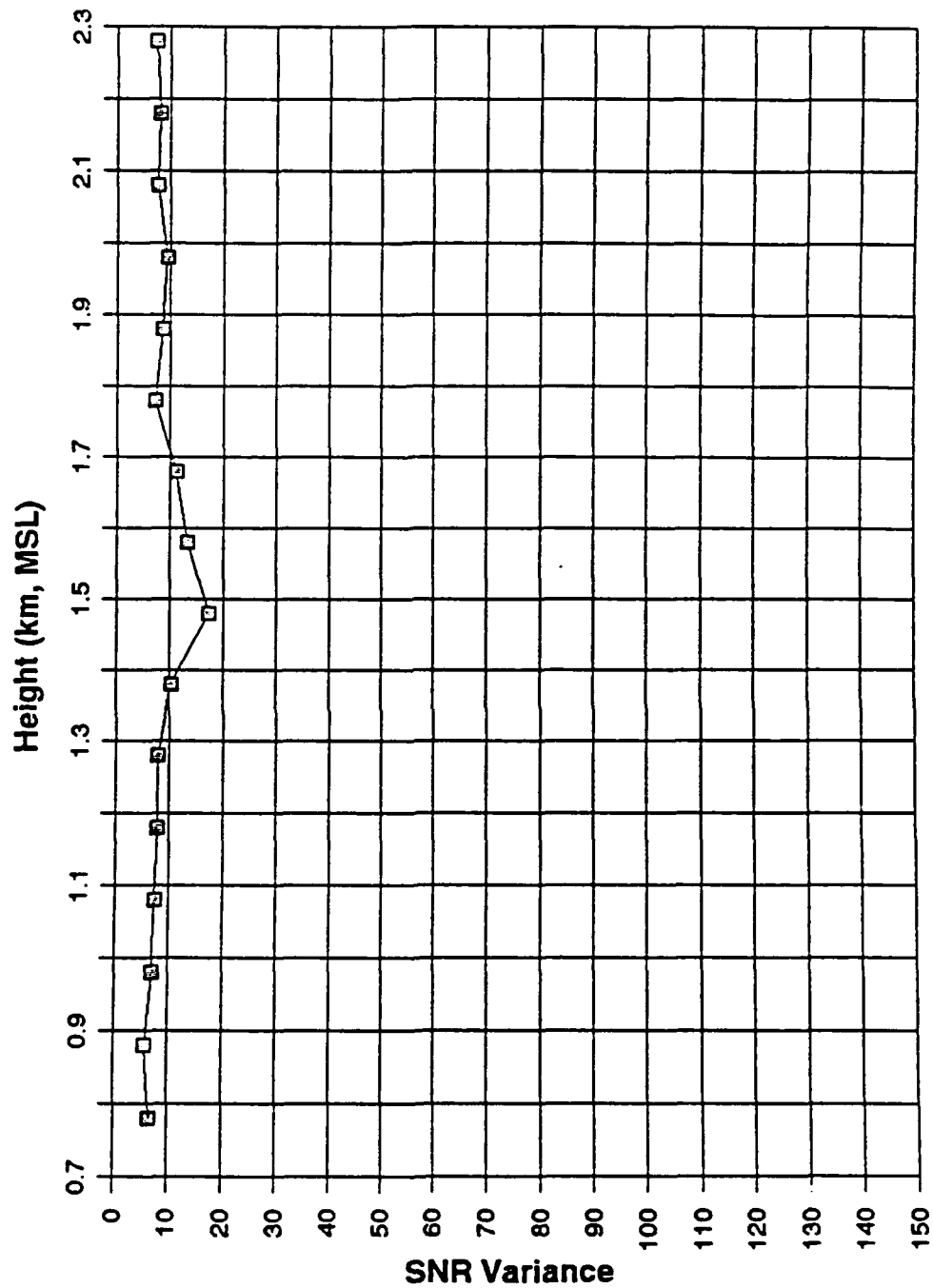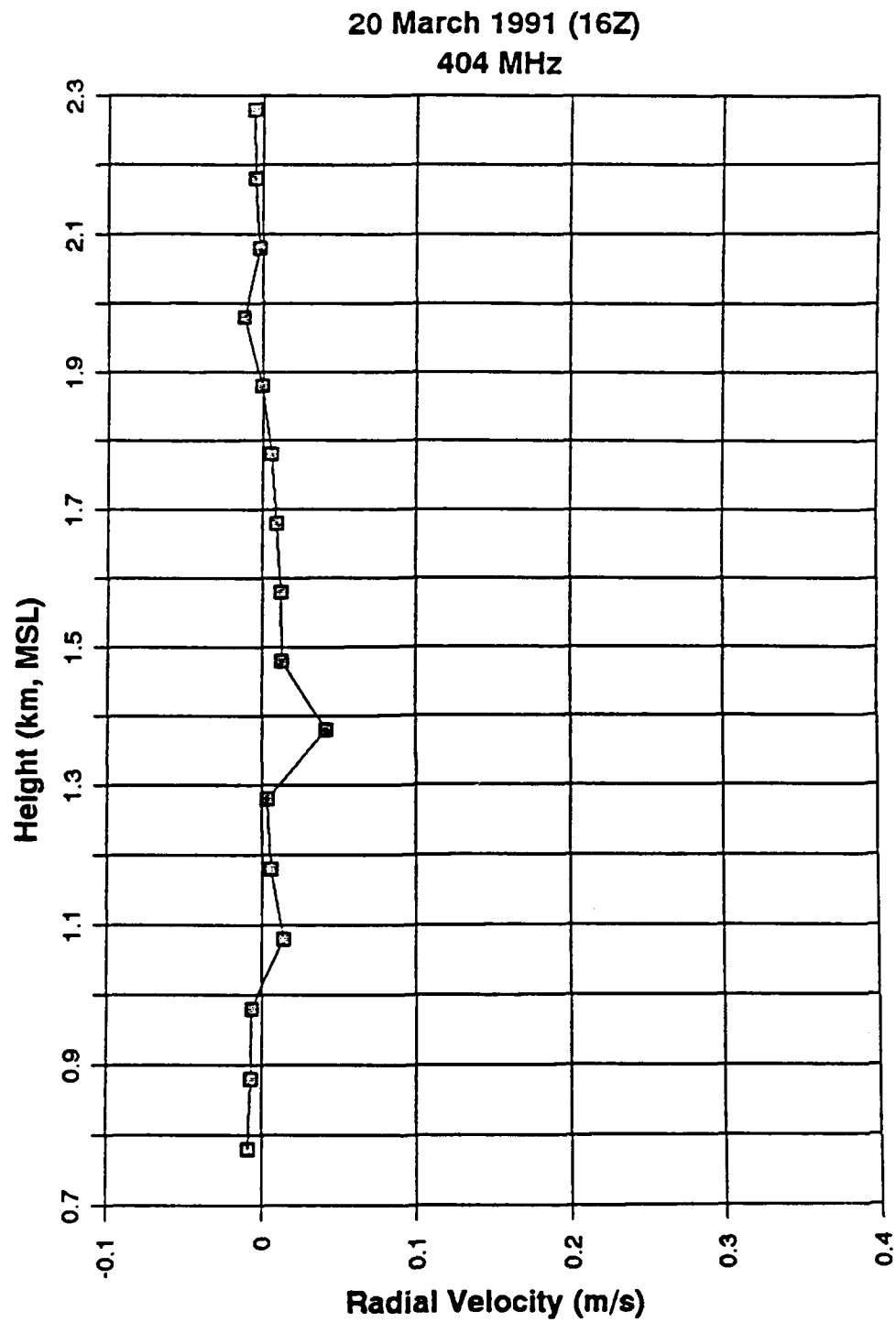Figure 4.29   Variance of SNR for 20 Mar 91, 15 Z

**20 March 1991 (16Z)**
**404 MHz**



Figure 4.30   Radial velocity from the 404 MHz profiler,
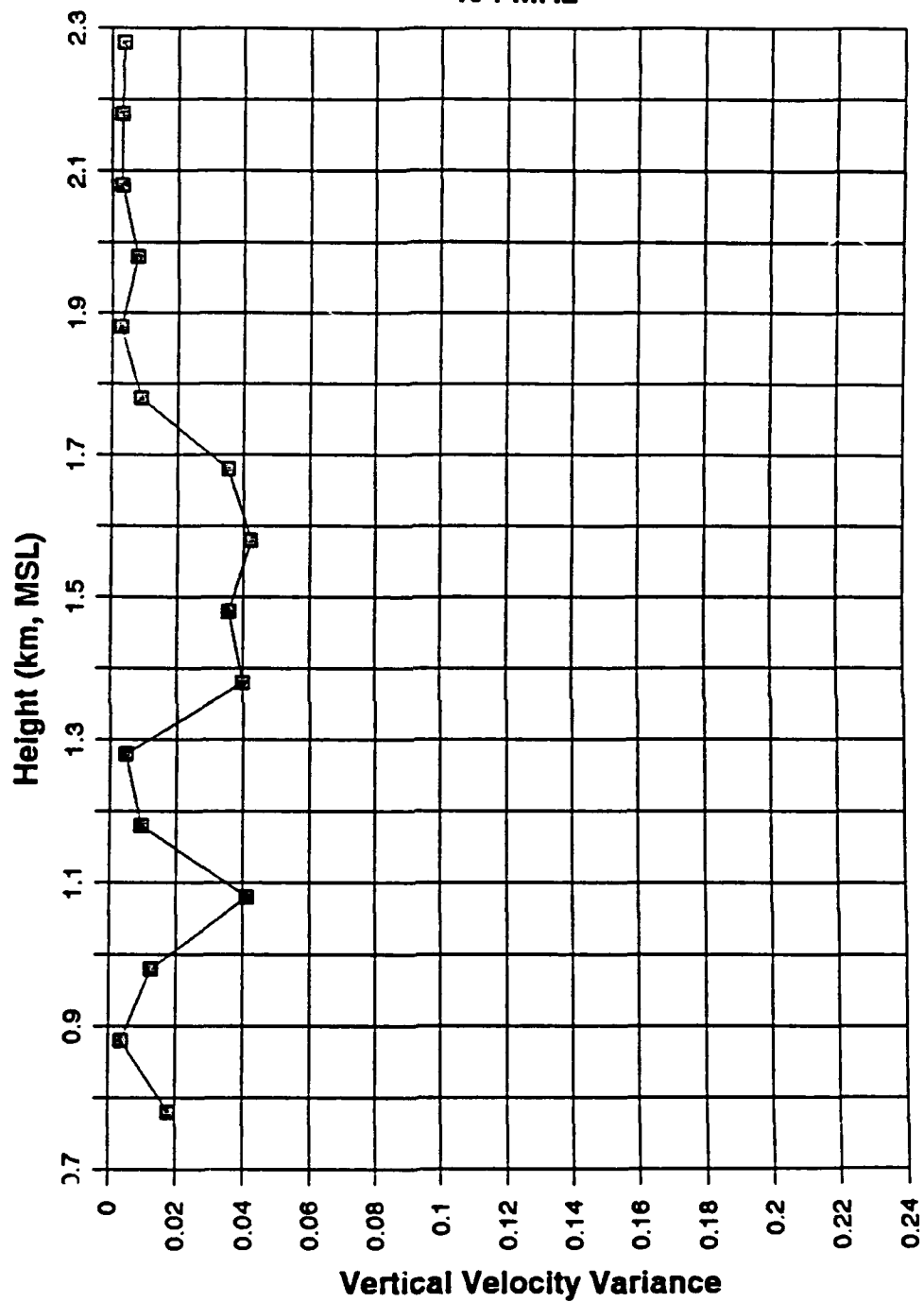              20 Mar 91, 16 ?

Figure 4.31    Variance in 404 MHz vertical velocities,
20 Mar 91, 16 Z

cloud cover. Ceilometer measurements indicated an average cloud cover of 23% for this period. Slight upward vertical motion is present in the lowest three gates as a result of increased surface heating and the resulting preferential, high reflectivity sampling of convective updrafts. Ceilometer indicates mean cloud base at 1510 m and radiosonde top at 1550 m. Cloud thickness (40 m) has reduced substantially to a layer thinner than the vertical resolution of the sampling volume of the profiler (100 m). A slight subsidence peak of 4 cm/s occurs at 1.38 km, still indicative of the presence of highly reflective, convectively cooled, descending air from inverted plumes at cloud top.

There is a broad peak in vertical velocity variance centered about 1.48 km. The breadth of this peak results from the rise in the inversion through several gates during the hour. The sampling volumes appear to enter and exit the clouds both spatially and temporally as a result of increasing inversion heights and dwindling cloud cover. A secondary peak in vertical velocity variance also appears at 1.08 km as a result of the increased surface heating. The estimated 16 Z inversion base is at 1550 m, this secondary variance peak occurs at 0.7 $z_i$. With surface heating effects included, Moeng (1986), in her LES simulations, identified variance peaks at 0.6 $z_i$ and, with no surface buoyancy, vertical velocity variance peaks at 0.7 $z_i$. However, the height of these peaks in variance were dependent on the relative

strength between surface buoyancy and cloud top convective cooling.

Chapter 5

SUMMARY, CONCLUSIONS, AND SUGGESTIONS FOR FUTURE WORK

## 5.1  Summary and Conclusions

High temporal measurements of vertical velocity were collected from wind profilers in a cloudy convective boundary layer over land.  The data were used to determine the cloud and sub-cloud vertical velocity structure and to evaluate the performance of wind profilers in a cloudy convective boundary layer over land.  The 915 MHz profiler proved to be very sensitive to precipitation.  Initial (20 March 1991) data were biased as a result of zero suppression filtering.  In the absence of zero suppression filtering, horizontal wind contamination also biased the 915 MHz vertical velocity measurements of 31 January 1992.  As a result, vertical velocity data from the 915 MHz profiler were deemed unsuitable for this study.

The 404 MHz profiler provided useful, high temporal data on 20 Mar 91.  Peaks in vertical velocity and vertical velocity variance were evident at cloud top, and as the sky cleared, a second peak in vertical velocity variance occurred at about 0.7 $z_i$.  The increased mean and variance profiles were the result of cloud top convective instability causing sinking motions (inverted plumes) which were preferentially sampled in the radar beam.  Preferential sampling was possibly

the result of highly reflective air in the inverted plume from a large $C_n^2$. A high $C_n^2$, within the inverted plume, was the result of entrained free atmosphere air mixing with the boundary layer air. An alternative possibility for this high reflectivity may have been the result of conditional sampling of frozen precipitation particles at cloud top.

In the presence of an undulating cloud top, the sampling volume may be above or below cloud top and continue to preferentially measure increased vertical velocities and variances. This hypothesis is further supported by SNR measurements at cloud top. Signal-to-noise ratio in a volume where measurements are preferentially sampled in clear air, at cloud top, would tend to have a reduced average SNR, and an increased SNR variance.

Transition to a clear-sky convective boundary layer was characterized by a decreased mean subsidence as time progressed. Increased solar heating reduced the mean downward vertical velocities as a result of preferential sampling of highly reflective upward vertical velocities. Upward rising plumes of surface air carried similar $C_n^2$ properties to that of the inverted plumes, and are more reflective than the surrounding boundary layer air. By 16 Z, in the lowest three gates, slight mean upward vertical velocities were observed. In addition, 16 Z variance in vertical velocities showed two peaks as the sky cleared. A broad peak at cloud top was observed as a result of dwindling cloud cover. The second

peak, at about 0.7 $z_i$, was possibly the result of increased surface heating.

Mean cloud top was identifiable with high temporal resolution wind profilers as a peak in vertical velocity variance. Peaks in the variance of vertical velocities were observed either as a result of cloud-top radiative cooling, generating inverted plumes, or preferential sampling of undulating cloud top heights. Secondary peaks in vertical velocity variance below the cloud corresponded well with model results.

## 5.2 Suggestions for Future Work

When one measures clear-air (non-precipitating) vertical velocities with the 915 MHz profiler, the zero suppression filter must be removed in order to measure the vertical velocities on the scale of clear air vertical motions. Biases from horizontal wind contamination can be removed from the data by statistical analysis. Horizontal wind contamination could be minimized as follows:

1. Construct a permanent concrete foundation for the 915 MHz profiler antennas, so that repeatable and accurate installations of antenna assemblies can be achieved. The concrete platform will help to eliminate diurnal variations in soil depth (e.g., frost heave), as well as provide a repeatable installation surface for mounting the antenna elements.

2. Measure horizontal wind speed and direction to correlate with the vertical velocity data for that same period, over several synoptic cycles to eliminate random error. In order to solve for the zenith and azimuthal angle errors ($\phi$ and $\gamma$), one can correlate the horizontal component of the radial wind ($V_h \cos(\gamma-\theta)\sin(\phi)$) to the measured radial velocity ($V_r$). The hypothesis is that the correlation coefficient (r) between the measured radial velocity and its horizontal wind contribution will be highest and positive at that combination of $\gamma$ and $\phi$ which represent the angular bias in the wind profiler. Post processing can then remove the biased vertical velocities and reveal the unbiased vertical velocity values.

The use of high temporal vertical velocity information from wind profilers is an integral element in the study of cloud-topped convective boundary layers. Vertical winds at intervals of 30 seconds are able to resolve motions on the order of one minute. Sampling of horizontal winds from multi-beam wind profilers prohibit high temporal resolution vertical velocities. Longer time intervals between samples diminish temporal resolution, and as a result, the fine structure of vertical velocities in a convective boundary layer is lost.

In order to comprehensively study small-scale vertical motions in a convective boundary layer, a minimum instrument array should consist of the following: 1. radiosondes for thermodynamic and mean horizontal wind information. 2. unbiased, high temporal 404 MHz vertical velocity

measurements. 3. laser ceilometer data to determine cloud base height. 4. a 94 GHz cloud radar, in Doppler to determine cloud-top height and motions (entrainment, etc.).

A network array of wind profilers on the synoptic scale would be useful to determine large scale flow patterns (mean velocities, divergent flows, etc.). However, widely separated profilers alternately sampling both vertical and horizontal motions lose the high temporal advantage of fine scale vertical motion. The vertical motion microstructure in a cloud-topped boundary layer cannot be resolved, and like LES simulations, this subgrid-scale must be parameterized.

REFERENCES

Albrecht, B. A., A. K. Betts, W. H. Schubert and S.K. Cox, 1979: A model of the thermodynamic structure of the trade-wind boundary layer: Part I. theoretical formulation and sensitivity tests. J. Atmos. Sci., 36, 73-89.

Albrecht, B. A., R. S. Penc and W. H. Schubert, 1985: An observational study of cloud-topped mixed layers. J. Atmos. Sci., 42, 800-822.

Astling, E. G., 1976: Some aspects of cloud and precipitation features associated with a mid-latitude cyclone. Mon. Wea. Rev., 104, 1466-1473.

Barry, R. G. and R. J. Chorley, 1982: Atmosphere, Weather, and Climate, Methuen and Co. Ltd, 1982.

Battan, L. J., 1973: Radar Observation of the Atmosphere, The University of Chicago Press, 324 pp.

Bean, B. R., E. J. Dutton, 1966: Radio Meteorology, Dover Publications, Inc., 435 pp.

Brost, R. A., D. H. Lenschow and J.C. Wyngaard, 1982: Marine stratocumulus layers. Part I: Mean conditions. J Atmos. Sci., 39, 800-817.

Brownlee, K. A., 1965: Statistical Theory and Methodology in Science and Engineering, John Wiley and Sons, Inc., 590 pp.

Caughey, S. J., B. A. Crease and W. T. Roach, 1982: A field study of nocturnal stratocumulus II. Turbulence structure and entrainment. Quart. J. Roy. Meteor. Soc., 108, 125-144.

Caughey, S. J. and M. Kitchen, 1984: Simultaneous measurements of the turbulent and microphysical structure of nocturnal stratocumulus cloud. Quart. J. Roy. Meteor. Soc., 110, 13-34.

Deardorff, J. W., 1980: Stratocumulus-capped mixed layers derived from a three-dimensional model. Bound.-Layer Meteor., 18, 495-527.

Hignett, P., 1991: Observations of diurnal variation in a cloud-capped marine boundary layer. J. Atmos. Sci., 48, 1474-1482.

Keeler, R. J., R. E. Passarelli, 1990: Signal processing for atmospheric radars. Radar in Meteorology, D. Atlas, Ed., Amer. Meteor. Soc., 199-234.

Lenschow, D. H., J. C. Wyngaard and W.T. Pennell, 1980: Mean-field and second moment budgets in a baroclinic, convective boundary layer. J Atmos Sci., 31, 1313-1326.

Lilly, D. K., 1968: Models of cloud-topped mixed layers under a strong inversion. Quart. J. Roy. Meteor. Soc., 94, 292-309.

Nicholls, S., 1984: The dynamics of stratocumulus: aircraft observations and comparisons with a mixed layer model. Quart. J. Roy. Meteor. Soc., 110, 783-820.

Moeng, C. -H., 1986: Large-eddy simulation of a stratus-topped boundary layer. Part I: Structure and budgets. J. Atmos. Sci., 43, 2886-2900.

Moeng, C. -H., 1987: Large-eddy simulation of a stratus-topped boundary layer. Part II: Implications for mixed-layer modeling. J. Atmos. Sci., 44, 1605-1614.

Ottersten, H., 1969: Radar backscattering from the turbulent clear atmosphere. Radio Sci., 4, 1251-1255.

Richter, J. H., 1969: High resolution tropospheric radar sounding. Radio Sci., 4, 1261-1268.

Roach, W. T., R. Brown, S. J. Caughey, B. A. Crease and A. Slingo, 1982: A field study of nocturnal stratocumulus I. Mean structure and budgets. Quart. J. Roy. Meteor. Soc., 108, 103-123.

Rogers, R. R. and M. K. Yau, 1989: A short course in cloud physics. Pergamon Press., 290 pp.

Schubert, W. H., 1976: Experiments with Lilly's cloud-topped mixed layer model. J. Atmos. Sci., 33, 436-446.

Schubert, W. H., J. S. Wakefield, E. J. Steiner, and S. K. Cox, 1979: Marine stratocumulus convection. Part I: Governing equations and horizontally homogeneous solutions. J. Atmos. Sci., 36, 1286-1307.

Slingo, A., R. Brown and C. L. Wrench, 1982: A field study of nocturnal stratocumulus III. High resolution radiative and microphysical observations. Quart. J. Roy. Meteor. Soc., 108, 145-165.

Stull, R. B., 1988: _An Introduction to Boundary Layer Meteorology_, Kluwer Academic Publishers., 666 pp.

Underwood, K. H., 1981: Sodar signal processing methods and the RISo 78 experiment. PhD thesis, Dept. of Meteorology, Penn State, University Park, PA 16802, 175 pp.

VanZandt, T. E., J. L. Green, K. S. Gage, and W. L. Clark, 1978: Vertical profiles of refractivity turbulence structure constant: Comparison of observations by the Sunset Radar with a new theoretical model. _Radio Sci._, 13, 819-829.

Williams, S. R. and D. W. Thomson, 1986: An evaluation of errors observed in the measurement of low wind velocities. _Middle Atmosphere Program, Handbook for MAP_, 20, 256-262.